

Electrokinetic and aspect ratio effects on secondary flow of viscoelastic fluids in rectangular microchannels

M. Reshadi¹ · M. H. Saidi¹ · B. Firoozabadi¹ · M. S. Saidi¹

Received: 2 May 2016 / Accepted: 21 July 2016 / Published online: 3 August 2016
© Springer-Verlag Berlin Heidelberg 2016

Abstract The secondary flow of PTT fluids in rectangular cross-sectional plane of microchannels under combined effects of electroosmotic and pressure driving forces is the subject of the present study. Employing second-order central finite difference method in a very refined grid network, we investigate the effect of electrokinetic and geometric parameters on the pattern, strength and the average of the secondary flow. In this regard, we try to illustrate the deformations of recirculating vortices due to change in the dimensionless Debye–Hückel and zeta potential parameters as well as channel aspect ratio. We demonstrate that, in the presence of thick electric double layers, significant alteration occurs in the secondary flow pattern by transition from favorable to adverse pressure gradients. Moreover, it is found that for polymer-electrolyte solutions with large Debye lengths, the secondary flow pattern and the shape of vortices are generally dependent upon the width-to-height ratio of the channel cross section. Also, the inspections of strength and average of secondary flow reveal that the sensitivity of these quantities with respect to the electrokinetic, geometric and rheological

parameters increases by increasing the absolute value of velocity scale ratio. In this regard, utilizing the curve fitting of the results, several empirical expressions are presented for the strength and average of the secondary flow under various parametric conditions. The obtained relations with the other predictions for secondary flow are of high practical importance when dealing with the design of microfluidic devices that manipulate viscoelastic fluids.

Keywords Microfluidics · Electrokinetics · Viscoelasticity · Secondary flow · PTT model

List of symbols

APG/FPG	Adverse/favorable pressure gradient
C, F	Coefficient functions
\mathbf{D}	Rate of deformation tensor (s^{-1})
e	The charge of electron (C)
E_z	z-component of electric field (Vm^{-1})
El	Elasticity number
EOF	Electroosmotic flow
$f(\tau_{kk})$	PTT stress coefficient function
k_B	Boltzmann constant ($1.3807 \times 10^{-23} \text{JK}^{-1}$)
$L, 2H, 2W$	Microchannel length/height/width (m)
n_0	Ionic number concentration (m^{-3})
N_1	First normal stress difference
N_2	Second normal stress difference
p	Pressure (Pa)
Re	Reynolds number
t	Time (s)
T_m	Average absolute temperature (K)
\mathbf{u}	Velocity vector (ms^{-1})
Wi	Weissenberg number
x, y, z	Transverse/depthwise/axial coordinate (m)
\mathbb{Z}^{\pm}	Valence of ions

✉ M. H. Saidi
saman@sharif.edu
M. Reshadi
reshadi@mech.sharif.edu
B. Firoozabadi
firoozabadi@sharif.edu
M. S. Saidi
mssaidi@sharif.edu

¹ Center of Excellence in Energy Conversion (CEEC), School of Mechanical Engineering, Sharif University of Technology, Tehran 11155-9567, Iran

Greek symbols

α	Channel aspect ratio
Γ	Ratio of PD to HS velocities
ε	Extensibility parameter
ϵ	Dielectric constant of the fluid ($\text{CV}^{-1}\text{m}^{-1}$)
ϕ/Φ	External/total electrical potential (V)
η_p	Polymer viscosity coefficient (Pa s)
κ	Debye–Hückel parameter (m^{-1})
K	Dimensionless Debye–Hückel parameter
λ	Relaxation time (s)
ξ	PTT model parameter
ρ_e	Electric charge density (Cm^{-3})
τ, τ_{kk}	Polymeric/trace of extra stress tensor (Pa)
τ_{xz}, τ_{yz}	Streamwise shear stresses (Pa)
τ_{xx}, τ_{yy}	Transverse normal stresses (Pa)
τ_{xy}	Transverse shear stress (Pa)
τ_{zz}	Streamwise normal stress (Pa)
φ	Stream function (m^2s^{-1})
ψ, ψ_0	EDL/wall zeta potential (V)
Ω	Vorticity function (s^{-1})

Subscripts

i, j, k	Transverse/depthwise/axial direction
HS	Helmholtz–Smoluchowski
P, NB	Central node and neighbor grid point
PAA	Polyacrylamide solution
PTT	Phan–Thien–Tanner model

Superscripts

T	Transpose of the matrix
–	Relevant to dimensionless variable
□	Gordon–Schowalter convected derivative

1 Introduction

Microfluidics is usually used to analyze biochemical processes on lab-on-a-chip (LOC) devices (Bilitewski et al. 2003; Chow 2002; Figeys and Pinto 2000). In these systems, electroosmotic pump is considered as one of the most common ways for generating fluid flow in the microchannels due to ease of fabrication, precise flow control, etc. (Squires and Quake 2005). The origin of electroosmosis lies in the formation of electric double layer (EDL) due to the interaction between an electrolyte solution and an electrically charged surface. For microchannels with dielectric walls, due to the electroneutrality principle, the accumulation of counterions in the electrolyte solution near the fluid–solid interface forms the EDL. Then, by applying an external electric field in the channel axial direction, the mobile counterions through EDL are induced to move, by which a viscous drag force is exerted on the liquid, and subsequently, electroosmotic flow (EOF) is generated (Li

2004). Electroosmotic pump may work against a hydrodynamic load, e.g., due to the unequal pressure head of reservoirs (Berli 2010), or may be accompanied by another pumping mechanism (Vakili et al. 2014).

For the case of Newtonian fluids, the combined electroosmotic (EO) and pressure-driven (PD) flows result from the linear superposition of these two driving forces, for which lots of theoretical and computational studies have contributed to elucidate such velocity profile through microchannels with various geometries like slit, circular, annular and rectangular cross sections (see the review of Dutta and Beskok 2001). However, it has been demonstrated that biofluids like blood (Bodnár et al. 2011; Brust et al. 2013), saliva (Haward et al. 2011) and DNA solutions (Kolodner 1998) that are used in LOCs for biochemical analysis exhibit extraordinary behavior due to the emergence of some phenomena such as stress relaxation and shear-thinning properties. In this regard, different rheological models such as Casson (Ng 2013), Carreau (Zimmerman et al. 2006), power law (Babaie et al. 2011, 2012; Vakili et al. 2012, 2014), Maxwell (Ghosh and Chakraborty 2015; Jian et al. 2011) and Phan–Thien–Tanner (PTT) models (Park and Lee 2008b) have been proposed to take into account the non-Newtonian properties of these biofluids in the equations of motion through microchannels. However, the experimental data obtained from the flow measurement of blood (Owens 2006; Yeleswarapu et al. 1998) and human saliva (Vissink et al. 1984) demonstrated that, depending on the chemical constituents of these biofluids, there is some extent of viscoelasticity. In this regard, among various constitutive relations of viscoelastic model, the PTT equation is widely accepted for describing the related non-Newtonian properties of these complex biological fluids.

Using the simplified PTT (sPTT) constitutive equation (Phan–Thien 1978; Thien and Tanner 1977), Afonso et al. (2009) theoretically showed that, in contrast to Newtonian fluids, there is an additional contribution arising from the coupling between the electric and pressure potentials which avoids the superposition of two driving forces in combined EO/PD flows through slit microchannels. Other theoretical studies in the case of electroosmotic flow of PTT fluids through parallel plate microchannels have been pursued by considering the effect of surface hydrophobicity (Afonso et al. 2014), asymmetry in wall zeta potentials (Afonso et al. 2011) and wall depletion of additives (Sousa et al. 2011). Also, by extending the work of Afonso et al. (2009), Dhinakaran et al. (2010) obtained an analytical solution for 1D velocity profile of PTT fluids and, also, derived the equations for maximum electrical potential and the critical shear rates related to electroviscous stability of the PTT fluids.

From the macroscopic point of view, it has been well known that the presence of a nonzero second normal stress

difference (N_2) leads to the emergence of transverse recirculation in the case of pipes of non-circular cross sections, so that a secondary flow occurs in the plane perpendicular to the axial flow (Hashemabadi and Etemad 2006; Xue et al. 1995). In fact, due to the unequal normal stress components acting on orthogonal faces of the fluid element, a necessary but not sufficient condition is provided to induce the secondary flows through straight channels (Oldroyd 1958, 1965). In addition to experimental investigations (Debbaut et al. 1997; Debbaut and Dooley 1999; Townsend et al. 1976), a large number of theoretical and computational studies have been devoted to secondary flows of viscoelastic fluids through various channel geometries by using different constitutive models (Mai-Duy and Tanner 2005; Ramachandran and Leighton 2008; Siline and Leonov 2001; Tanoue et al. 2006). A comprehensive review and a general criterion on the direction of the secondary flow in macroscale pipes of noncircular cross section can be found in Yue et al. (2008). It has been demonstrated that, despite their inherently weak magnitude compared with the axial flow, the viscoelastic secondary flows in macroscale geometries may produce considerable effects in two fluid interface deformation (Debbaut et al. 1997) and heat transfer (Syrjälä 1998).

Separation of particles (Bhagat et al. 2008), size-based sorting (Chatterjee 2011; Yoon et al. 2009) and detection of the biological fluids components (Doddabasavana et al. 2012) are considered as the pivotal applications of the secondary flows in lab-on-a-chip microsystems. According to the absence of external forces, secondary flows induced by the modification of the channel geometry (Huang et al. 2004) or flow characteristics (Maenaka et al. 2008) are categorized as passive particle separation methods. The recent experiments studying the hydrodynamics of microparticles in microfluidic devices utilizing the secondary flows have demonstrated the excellent performance of these passive particle separation techniques (Chung et al. 2013). There are different types of geometries employed in inertial microfluidics to generate the secondary flows, such as serpentine (Di Carlo et al. 2008), spiral (Bhagat et al. 2008) and expansion–contraction array channels (Zhang et al. 2013). However, microchannels with linear structure are more in favor of channel parallelization and fabrication costs.

Passive cross-flow movement and patterning of microparticles in straight microchannels can be achieved by either inertial effects of particles (e.g., centrifugal forces Di Carlo et al. 2007) or suspending particles in viscoelastic fluids. The viscoelasticity-induced migration is the result of a non-uniform distribution of the first normal stress difference (N_1) in the microchannel providing a transversal driving force on the particles (D'Avino et al. 2012). For a flowing viscoelastic medium with negligible N_2 , no secondary

flows occur, and depending on their initial positions, the particles are driven toward the channel centerline and the closest corner of the microchannel (Nam et al. 2012), while, for viscoelastic fluids with nonzero N_2 , the migration of particles is shown to be significantly disturbed by the secondary flows, and their equilibrium positions and trajectories may be altered in accordance with secondary vortices structure (Lim et al. 2014). This implies the fact that, although the strength of the secondary flows is orders of magnitude lower than the primary flow velocity, it may be comparable to the lateral migration velocity of particles (Villone et al. 2013). On the other hand, the shape of the vortex structure of the secondary flows depends on the type of the flow driving force. For the case of pressure-driven flows, it is well known that only two secondary vortices are generated in the cross-sectional plane of the channel (Yue et al. 2008). However, with the advent of new pumping mechanisms such as electroosmotic pump, understanding the secondary flow physics under such driving force is mandatory in order to better control the trajectories of particles during the separation, counting and sorting processes in lab-on-a-chip microsystems.

To our knowledge, Park and Lee's paper (Park and Lee 2008a) is the only work which has presented a numerical study of the combined EO/PD flows of PTT fluids through straight microchannels with square cross section considering three-dimensional velocity field. In Park and Lee's work, the investigation of secondary flow of PTT fluids under combined effect of electroosmosis and hydrodynamics is done under limited circumstances, in which the channel aspect ratio and all electrokinetic parameters such as wall zeta potential and the Debye length were kept constant, and the parametric studies were confined to the case of favorable pressure gradients (FPG) and the infinitesimal Debye length (i.e., less than one thousandth of the channel width). However, the thickness of Debye layer is very significant for the cases of low ionic concentration of the electrolyte solution (Yang and Li 1997), especially when the channel size is scaled down to micron and submicron levels (Horiuchi and Dutta 2006). Thus, the dependence of the recirculation on the electrokinetic parameters and, also, the shape of the secondary flow under adverse pressure gradients (APG) remain unclear. As mentioned above, the difference between the transverse normal stress components is responsible for inducing secondary flow. Also, as shown by Dhinakaran et al. (2010), the normal stress components of the PTT fluids in electroosmotic flows are affected by the Debye–Hückel parameter. So, it is expected that the electrokinetic parameters play a key role in the pattern and the strength of the secondary flow. On the other hand, the effect of channel geometry on secondary flow of viscoelastic fluids in the macroscale domain has been reported by several authors (Gervang and Larsen 1991; Hashemabadi and

Etemad 2006; Poole et al. 2013; Xue et al. 1995; Yue et al. 2008). But, to the best of our knowledge, the effect of channel aspect ratio on the secondary flow through rectangular microchannels (as widely used in the microfluidic applications) in the presence of the electrokinetic phenomena has not been investigated in the literature so far.

Since a precise design of microfluidic systems requires the effort to consider the effect of all aforementioned parameters on the flow patterns, the present study addresses the influence of channel aspect ratio, wall zeta potential and the Debye–Hückel parameter on the shape, average and strength of the secondary flow of a PTT viscoelastic fluid through rectangular microchannels when subjected to the electroosmotic and adverse/favorable pressure driving forces. At first, in order to understand the profile of the secondary flow under different values of control parameters, the combined EO/PD flows are simulated by numerically solving the set of nonlinear Poisson–Boltzmann (PB), Cauchy momentum and the complete form of PTT constitutive equations based on finite difference method (FDM). In this regard, the stream function approach is used to formulate the coupled momentum and continuity equations. Afterward, the discretized form of the differential equations for the electrical potential, stream function and axial velocity component are solved with the appropriate boundary conditions via the Gauss–Seidel iterative algorithm. Finally, the influence of rheological properties and electrokinetic parameters on average and strength of the secondary flows is investigated over a wide range of operating parameters.

The rest of the paper is arranged as follows: In Sect. 2, the flow geometry is elucidated and the physical description

of the problem and assumptions is expressed. The description of the governing equations, boundary conditions, model formulation and non-dimensionalization is given in Sect. 3. Numerical analysis of the electric potential, the velocity and stress fields is conducted in Sect. 4. After validating and discussing the results in Sect. 5, we end by summarizing our key scientific findings in Sect. 6.

2 Physical description of the problem and assumptions

We consider steady, laminar ($Re < 1$), fully developed and incompressible flow of a viscoelastic fluid through a straight rectangular microchannel, as schematically shown in Fig. 1. x , y and z denote the channel's cross-stream, depthwise and axial coordinates, respectively, in which the primary flow is in the z direction and the secondary flow occurs in the $x - y$ plane. The coordinate origin is located at the center of the plane far enough from the inlet of the channel, and the axial length of the channel is L . The depth and width of the microchannel are $2H$ and $2W$, respectively, which are considered to be much smaller than L . The channel walls are subject to uniform and constant zeta potential. The fluid rheologically obeys the complete single-mode Phan-Thien–Tanner (PTT) constitutive equation with the linear stress coefficient function in the absence of a solvent viscosity contribution. Also, the fluid is electrochemically an ideal solution of fully dissociated symmetric salts.

The basic principles of electroosmosis are briefly discussed in Sect. 1, and the detailed theoretical background

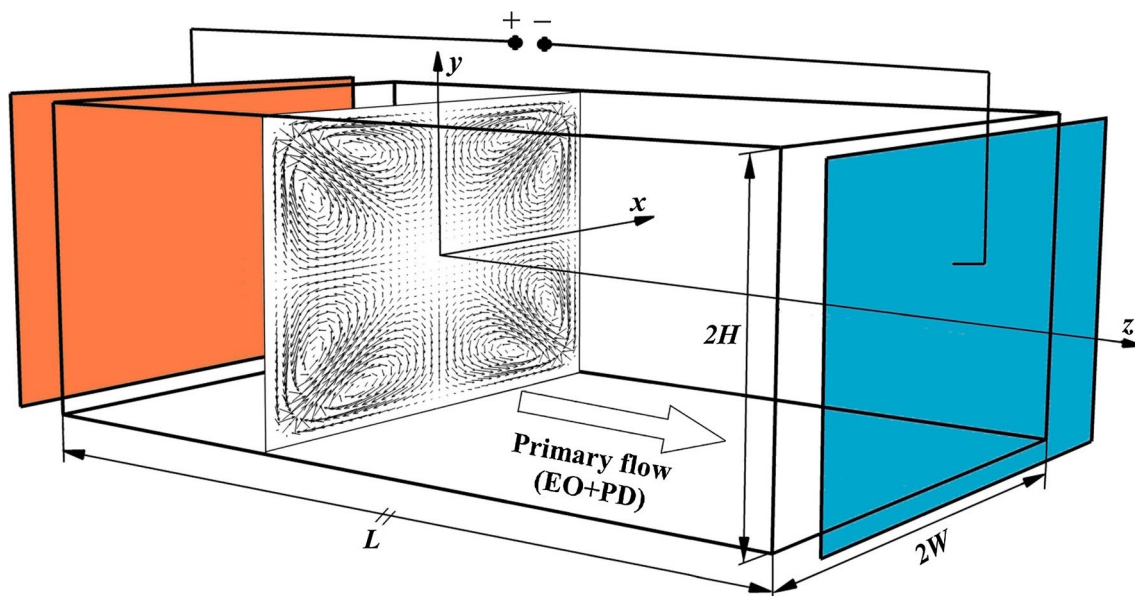


Fig. 1 Schematic representation of combined EO/PD flows of a viscoelastic fluid (including secondary flow) in a rectangular microchannel with relevant coordinates system

can be found in numerous books (Karniadakis et al. 2006; Li 2004) and papers (Babaie et al. 2011, 2012; Sadeghi et al. 2014). Here, we recall its physical concept for the present problem. As shown in Fig. 1, by applying the DC electrical potential via the anode (red plate) and cathode (blue plate) electrodes, the mobile counterions in the EDL are induced to move, by which a viscous drag force is exerted on the fluid and the EOF is generated. Also, due to the presence of an additional pumping mechanism or the difference in the column height between the reservoirs, the EOF may be accompanied by a favorable or adverse pressure gradient. In the present study, the primary flow along the axial direction is driven by the EO force combined with a constant pressure gradient. Due to fully developed flow condition, all variables are independent from z . Also, all thermo-physical properties of the fluid are assumed to be constant and expressed in the absolute average temperature of the fluid. It should be noted that, due to symmetry, the analysis is limited to the upper-right quadrant of the channel cross section.

3 Governing equations and boundary conditions

The combined EO and PD flows of a viscoelastic fluid are governed by the set of conservation of ions, mass, momentum and the fluid constitutive equations. The continuity and Cauchy momentum equations for the incompressible and fully developed flow conditions are described as follows:

$$\frac{\partial u_x}{\partial x} + \frac{\partial u_y}{\partial y} = 0 \tag{1}$$

$$\rho \left(u_x \frac{\partial u_x}{\partial x} + u_y \frac{\partial u_x}{\partial y} \right) = -\frac{\partial p}{\partial x} + \left[\frac{\partial \tau_{xx}}{\partial x} + \frac{\partial \tau_{xy}}{\partial y} \right] \tag{2}$$

$$\rho \left(u_x \frac{\partial u_y}{\partial x} + u_y \frac{\partial u_y}{\partial y} \right) = -\frac{\partial p}{\partial y} + \left[\frac{\partial \tau_{yx}}{\partial x} + \frac{\partial \tau_{yy}}{\partial y} \right] \tag{3}$$

$$\rho \left(u_x \frac{\partial u_z}{\partial x} + u_y \frac{\partial u_z}{\partial y} \right) = -\frac{\partial p}{\partial z} + \left[\frac{\partial \tau_{zx}}{\partial x} + \frac{\partial \tau_{zy}}{\partial y} \right] + \rho_e E_z \tag{4}$$

where u_x, u_y and u_z are the components of velocity vector \mathbf{u} , p is the pressure, and E_z is the externally applied electric field along the axial direction. Also, τ_{ij} is the polymeric extra stress tensor components governed by the constitutive equation of the PTT model, and ρ_e is the net electric charge density being obtained later from the PB equation.

3.1 Poisson–Boltzmann equation

The net electric charge density, ρ_e , in the EDL can be related to the total potential field (Φ) by the Poisson equation as follows:

$$\nabla^2 \Phi = -\frac{\rho_e}{\epsilon} \tag{5}$$

where ϵ is the dielectric constant of the solution. The total electric field ($\Phi = \phi + \psi$) is given by a linear superposition of the applied electric field generated by the electrodes, $\phi(z)$, and electric field due to the net charge distribution in the EDL, $\psi(x, y)$. By interpreting the above equation with the standard electrokinetic model (Li 2004), the RHS of Eq. (5) becomes a function of two variables, x and y . So by substituting $\Phi = \phi + \psi$, Eq. (5) can be separated into the two following equations:

$$\nabla^2 \psi = -\frac{\rho_e}{\epsilon}, \quad \nabla^2 \phi = 0 \tag{6}$$

Therefore, the net electric charge density is independent from the external electric field and is determined by ψ . According to the quasi-equilibrium conditions, the ion density variation in the EDL obeys the Boltzmann distribution. So, for a symmetric electrolyte of equal valence ($\mathbb{Z} = \mathbb{Z}^+ = -\mathbb{Z}^-$), the explicit form of the first part in Eq. (6) can be expressed by the PB equation as follows:

$$\nabla^2 \psi = \frac{1}{\epsilon} \left[2e\mathbb{Z}n_0 \sinh \left(\frac{e\mathbb{Z}\psi}{k_B T_m} \right) \right] \tag{7}$$

where n_0 is the bulk number concentration of ions in the electrolyte solution, T_m is the absolute average temperature, k_B is the Boltzmann constant, and e is the elementary electronic charge. So, the potential field of the electric double layers with associated boundary conditions in (x, y) coordinates can be expressed as:

$$\begin{cases} \frac{\partial^2 \psi}{\partial x^2} + \frac{\partial^2 \psi}{\partial y^2} = \frac{2e\mathbb{Z}n_0}{\epsilon} \sinh \left(\frac{e\mathbb{Z}\psi}{k_B T_m} \right) \\ \frac{\partial \psi}{\partial x} \Big|_{x=0} = \frac{\partial \psi}{\partial y} \Big|_{y=0} = 0, \psi|_{x=W} = \psi|_{y=H} = \psi_0 \end{cases} \tag{8}$$

where the electrical potential near the surface is considered to be equal to the zeta potential of the walls (ψ_0), and the symmetry conditions are used at the transverse coordinates. To generalize the above analysis, the following dimensionless quantities are defined:

$$\bar{x} = \frac{x}{H}, \bar{y} = \frac{y}{H}, \alpha = \frac{W}{H}, \bar{\psi} = \frac{e\mathbb{Z}\psi}{k_B T_m}, \bar{\psi}_0 = \frac{e\mathbb{Z}\psi_0}{k_B T_m}, K = \kappa H \tag{9}$$

where α is the channel aspect ratio and K is the dimensionless Debye–Hückel parameter being defined as $\kappa^2 = 2n_0 e^2 \mathbb{Z}^2 / \epsilon k_B T_m$. By using the above parameters, Eq. (8) can be rewritten in dimensionless form as:

$$\begin{cases} \frac{\partial^2 \bar{\psi}}{\partial \bar{x}^2} + \frac{\partial^2 \bar{\psi}}{\partial \bar{y}^2} = K^2 \sinh \bar{\psi} \\ \frac{\partial \bar{\psi}}{\partial \bar{x}} \Big|_{\bar{x}=0} = \frac{\partial \bar{\psi}}{\partial \bar{y}} \Big|_{\bar{y}=0} = 0, \bar{\psi} \Big|_{\bar{x}=\alpha} = \bar{\psi} \Big|_{\bar{y}=1} = \bar{\psi}_0 \end{cases} \tag{10}$$

So, independent from velocity and stress tensor, $\bar{\psi}$ can be evaluated by solving the above equation.

3.2 Constitutive equation of PTT model

We use the PTT model to simulate the shear-thinning behavior of the polymer solution with the following constitutive equation:

$$f(\tau_{kk})\boldsymbol{\tau} + \lambda \left(\frac{\square}{\boldsymbol{\tau}} \right) = 2\eta_p \mathbf{D} \tag{11}$$

where the above equation is expressed in terms of the polymer stress with the simplified notation $\boldsymbol{\tau}_p \equiv \boldsymbol{\tau}$. Also, $\tau_{kk} = \tau_{xx} + \tau_{yy} + \tau_{zz}$ represents the trace of the extra stress tensor. In addition, λ is the relaxation time of the fluid, η_p is the polymer viscosity coefficient, \mathbf{D} is the rate of deformation tensor, \square is the Gordon–Schowalter convected derivative of the stress tensor, and $f(\tau_{kk})$ is the linearized form of the stress coefficient function. The latter three cases are expressed by the following relations:

$$\mathbf{D} = (\nabla \mathbf{u} + \nabla \mathbf{u}^T)/2 \tag{12}$$

$$\square \boldsymbol{\tau} = \frac{D\boldsymbol{\tau}}{Dt} - \boldsymbol{\tau} \cdot \nabla \mathbf{u} - \nabla \mathbf{u}^T \cdot \boldsymbol{\tau} + \xi(\boldsymbol{\tau} \cdot \mathbf{D} + \mathbf{D} \cdot \boldsymbol{\tau}) \tag{13}$$

$$f(\tau_{kk}) = 1 + (\varepsilon \lambda / \eta_p) \text{tr} \boldsymbol{\tau} \tag{14}$$

In Eq. (13), parameter ξ accounts for the slip between the molecular network and the continuum medium (Thien and Tanner 1977), and in the case of $\xi = 0$, the Oldroyd’s upper convected derivative is recovered. It is noteworthy that for steady flows, $D\boldsymbol{\tau}/Dt = 0$. Also in Eq. (14), ε reflects the elongational viscosity. By applying ($\varepsilon = 0, \xi = 0$) ($\varepsilon = 0, \xi \neq 0$) and ($\varepsilon \neq 0, \xi = 0$), the above constitutive equation is reduced to the simplified Oldroyd-B model in the absence of retardation time (Vamerzani et al. 2014) (or the upper convected Maxwell model), Johnson–Segalman (Ireka and Chinyoka 2016) and the simplified PTT (sPTT) model, respectively. In the first two cases, the stress coefficient function is $f(\tau_{kk}) = 1$, and in the latter case, for fully developed flows, the constitutive equation of sPTT model can be converted to that of FENE-P model by the appropriate substitutions (Cruz et al. 2005; Oliveira 2002). To generalize the present problem, the tensorial form of the above equation is made dimensionless by using the following non-dimensional quantities:

$$\begin{aligned} \bar{\mathbf{u}} &= \frac{\mathbf{u}}{u_{HS}}, \quad \Gamma = -\frac{3u_{PD}}{u_{HS}}, \quad \bar{\nabla} = H\nabla, \\ \bar{\boldsymbol{\tau}} &= \frac{\boldsymbol{\tau}}{\eta_p u_{HS} / H}, \quad \text{Wi}_\kappa = \lambda u_{HS} \kappa \end{aligned} \tag{15}$$

where Γ is the ratio of characteristic pressure-driven flow (PDF) velocity ($u_{PD} = -H^2 p_{,z} / 3\eta_p$) to the

Helmholtz–Smoluchowski velocity (Park and Lee 2008b) ($u_{HS} = -\epsilon \psi_0 E_z / \eta_p$) and also can be expressed as $\Gamma = -\bar{\nabla} \bar{p}$ in which \bar{p} is the dimensionless pressure scaled with the characteristic viscous term $u_{HS} \eta_p / H$ (White and Corfield 2006). Also, $\Gamma < 0$ and $\Gamma > 0$ correspond to the cases of FPG and APG, respectively, and the cases of $\Gamma = 0$ and $\Gamma \rightarrow \infty$ are related to pure EO and pure PD flows, respectively. In addition, Wi_κ is the Weissenberg number based on the Debye–Hückel parameter and the Helmholtz–Smoluchowski velocity. So, the combination of Eqs. (11–14) can be written in the dimensionless tensorial form as:

$$f(\bar{\tau}_{kk})\bar{\boldsymbol{\tau}} + \frac{\text{Wi}_\kappa}{K} \left\{ -\bar{\boldsymbol{\tau}} \cdot \bar{\nabla} \bar{\mathbf{u}} - \bar{\nabla} \bar{\mathbf{u}}^T \cdot \bar{\boldsymbol{\tau}} + \xi [\bar{\boldsymbol{\tau}} \cdot \bar{\mathbf{D}} + \bar{\mathbf{D}} \cdot \bar{\boldsymbol{\tau}}] \right\} = 2\bar{\mathbf{D}} \tag{16}$$

where $\bar{\mathbf{D}} = (\bar{\nabla} \bar{\mathbf{u}} + \bar{\nabla} \bar{\mathbf{u}}^T) / 2$ and $f(\bar{\tau}_{kk}) = 1 + \varepsilon \text{Wi}_\kappa \text{tr} \bar{\boldsymbol{\tau}} / K$ are the dimensionless form of the rate of deformation tensor and the stress coefficient function, respectively.

3.3 Stream function representation for equations of motion

The two-dimensional secondary flow field in the cross-sectional plane of the microchannel can be obtained, using the stream function approach. If a dimensionless stream function $\bar{\varphi} = \varphi / Hu_{HS}$ is defined by the following equations:

$$\bar{u}_x = \frac{\partial \bar{\varphi}}{\partial \bar{y}}, \quad \bar{u}_y = -\frac{\partial \bar{\varphi}}{\partial \bar{x}} \tag{17}$$

the continuity Eq. (1) is automatically satisfied. So, the momentum equations in the x and y directions (Eqs. 2 and 3, respectively) can be combined by cross-differentiation to yield the following relation:

$$\frac{\partial \bar{\varphi}}{\partial \bar{x}} \frac{\partial \bar{\Omega}}{\partial \bar{y}} - \frac{\partial \bar{\varphi}}{\partial \bar{y}} \frac{\partial \bar{\Omega}}{\partial \bar{x}} = \frac{1}{\text{Re}} \left(\frac{\partial^2 \bar{\tau}_{xx}}{\partial \bar{x} \partial \bar{y}} - \frac{\partial^2 \bar{\tau}_{yy}}{\partial \bar{x} \partial \bar{y}} + \frac{\partial^2 \bar{\tau}_{xy}}{\partial \bar{y}^2} - \frac{\partial^2 \bar{\tau}_{xy}}{\partial \bar{x}^2} \right) \tag{18}$$

in which $\bar{\Omega} = -(\bar{\varphi}_{,xx} + \bar{\varphi}_{,yy})$ is the dimensionless vorticity function and $\text{Re} = \rho u_{HS} H / \eta_p$ represents the Reynolds number based on the Helmholtz–Smoluchowski velocity and the channel half-height. For the microflow of a typical viscoelastic fluid at 25°C in LOC devices, $H \sim 10^{-4} \text{m}$, $u_{HS} \sim 10^{-3} \text{ms}^{-1}$, $\rho \sim 10^3 \text{kg m}^{-3}$, $\eta_p \sim 10^{-3} \text{kg m}^{-1} \text{s}^{-1}$ (Park and Lee 2008a). Thus $\text{Re} \sim 10^{-1}$, and therefore, we have set $\text{Re} = 0.1$ throughout the paper for parametric study except at the experimental validation. As can be seen, the pressure terms are eliminated from the compact form of the momentum equations. Also, after substituting the obtained expression for the net electric charge density from Eq. (7) into Eq. (4), the dimensionless form of the momentum Eq. (4) in the z direction can be written as follows:

$$\bar{u}_x \frac{\partial \bar{u}_z}{\partial \bar{x}} + \bar{u}_y \frac{\partial \bar{u}_z}{\partial \bar{y}} = \frac{1}{\text{Re}} \left(-\Gamma + \frac{\partial \bar{\tau}_{zx}}{\partial \bar{x}} + \frac{\partial \bar{\tau}_{zy}}{\partial \bar{y}} + \frac{K^2}{\psi_0} \sinh \bar{\psi} \right) \tag{19}$$

After replacing the transverse velocity components with their equivalent derivatives of $\bar{\varphi}$, the dimensionless stress tensor components can be obtained from the expansion of Eq. (16) as follows:

$$\begin{aligned} \bar{\tau}_{xx} = & \Lambda_1 \left(2 \frac{\partial^2 \bar{\varphi}}{\partial \bar{x} \partial \bar{y}} + 2 \frac{\text{Wi}_k}{K} \frac{\partial^2 \bar{\varphi}}{\partial \bar{y}^2} \bar{\tau}_{xy} \right. \\ & \left. - \frac{\xi \text{Wi}_k}{K} \left[\frac{\partial^2 \bar{\varphi}}{\partial \bar{y}^2} - \frac{\partial^2 \bar{\varphi}}{\partial \bar{x}^2} \right] \bar{\tau}_{yx} \right) + I_1 \end{aligned} \tag{20}$$

$$\begin{aligned} \bar{\tau}_{yy} = & \Lambda_2 \left(-2 \frac{\partial^2 \bar{\varphi}}{\partial \bar{x} \partial \bar{y}} - 2 \frac{\text{Wi}_k}{K} \frac{\partial^2 \bar{\varphi}}{\partial \bar{x}^2} \bar{\tau}_{xy} \right. \\ & \left. - \frac{\xi \text{Wi}_k}{K} \left[\frac{\partial^2 \bar{\varphi}}{\partial \bar{y}^2} - \frac{\partial^2 \bar{\varphi}}{\partial \bar{x}^2} \right] \bar{\tau}_{yx} \right) + I_2 \end{aligned} \tag{21}$$

$$\begin{aligned} \bar{\tau}_{xy} = & \Lambda_3 \left(\left[\frac{\partial^2 \bar{\varphi}}{\partial \bar{y}^2} - \frac{\partial^2 \bar{\varphi}}{\partial \bar{x}^2} \right] \left[1 - \frac{\xi \text{Wi}_k}{2K} (\bar{\tau}_{xx} + \bar{\tau}_{yy}) \right] \right. \\ & \left. + \frac{\text{Wi}_k}{K} \left[-\frac{\partial^2 \bar{\varphi}}{\partial \bar{x}^2} \bar{\tau}_{xx} + \frac{\partial^2 \bar{\varphi}}{\partial \bar{y}^2} \bar{\tau}_{yy} \right] \right) - I_3 \end{aligned} \tag{22}$$

$$\begin{aligned} \bar{\tau}_{xz} = & \Lambda_4 \left(\left[1 - \frac{\text{Wi}_k}{2K} (\bar{\tau}_{xx} (\xi - 2) + \bar{\tau}_{zz} \xi) \right] \frac{\partial \bar{u}_z}{\partial \bar{x}} \right. \\ & \left. + \left[\frac{\text{Wi}_k}{2K} \bar{\tau}_{xy} (2 - \xi) \right] \frac{\partial \bar{u}_z}{\partial \bar{y}} \right) + I_4 \end{aligned} \tag{23}$$

$$\begin{aligned} \bar{\tau}_{yz} = & \Lambda_5 \left(\frac{\partial \bar{u}_z}{\partial \bar{y}} \left[1 - \frac{\text{Wi}_k}{2K} (\bar{\tau}_{yy} (\xi - 2) + \bar{\tau}_{zz} \xi) \right] \right. \\ & \left. + \left[\frac{\text{Wi}_k}{2K} \bar{\tau}_{xy} (2 - \xi) \right] \frac{\partial \bar{u}_z}{\partial \bar{x}} \right) + I_5 \end{aligned} \tag{24}$$

$$\bar{\tau}_{zz} = \Lambda_3 \frac{\text{Wi}_k}{K} (2 - \xi) \left[\frac{\partial \bar{u}_z}{\partial \bar{x}} \bar{\tau}_{xz} + \frac{\partial \bar{u}_z}{\partial \bar{y}} \bar{\tau}_{yz} \right] \tag{25}$$

where the parameters Λ_{1-5} and I_{1-5} are defined as follows:

$$\begin{aligned} \Lambda_1^{-1} = & f(\bar{\tau}_{kk}) + \frac{2\text{Wi}_k}{K} \frac{\partial^2 \bar{\varphi}}{\partial \bar{x} \partial \bar{y}} (\xi - 1), \quad \Lambda_2^{-1} = f(\bar{\tau}_{kk}) \\ & - \frac{2\text{Wi}_k}{K} \frac{\partial^2 \bar{\varphi}}{\partial \bar{x} \partial \bar{y}} (\xi - 1), \quad \Lambda_3^{-1} = f(\bar{\tau}_{kk}) \end{aligned} \tag{26}$$

$$\begin{aligned} \Lambda_4^{-1} = & f(\bar{\tau}_{kk}) + \frac{\text{Wi}_k}{K} \frac{\partial^2 \bar{\varphi}}{\partial \bar{x} \partial \bar{y}} (\xi - 1), \quad \Lambda_5^{-1} = f(\bar{\tau}_{kk}) \\ & - \frac{\text{Wi}_k}{K} \frac{\partial^2 \bar{\varphi}}{\partial \bar{x} \partial \bar{y}} (\xi - 1) \end{aligned} \tag{27}$$

$$\begin{aligned} I_1 = & \Lambda_1 \frac{\xi \text{Wi}_k}{K} \frac{\partial \bar{u}_z}{\partial \bar{x}} \bar{\tau}_{xz}, \quad I_2 = \Lambda_2 \frac{\xi \text{Wi}_k}{K} \frac{\partial \bar{u}_z}{\partial \bar{y}} \bar{\tau}_{yz}, \\ I_3 = & \Lambda_3 \frac{\xi \text{Wi}_k}{2K} \left[\frac{\partial \bar{u}_z}{\partial \bar{x}} \bar{\tau}_{yz} + \frac{\partial \bar{u}_z}{\partial \bar{y}} \bar{\tau}_{xz} \right] \end{aligned} \tag{28}$$

$$\begin{aligned} I_4 = & \frac{\text{Wi}_k}{2K} \Lambda_4 \bar{\tau}_{yz} \left[\frac{\partial^2 \bar{\varphi}}{\partial \bar{y}^2} (2 - \xi) + \frac{\partial^2 \bar{\varphi}}{\partial \bar{x}^2} \xi \right], \\ I_5 = & \frac{\text{Wi}_k}{2K} \Lambda_5 \bar{\tau}_{xz} \left[\frac{\partial^2 \bar{\varphi}}{\partial \bar{x}^2} (\xi - 2) - \frac{\partial^2 \bar{\varphi}}{\partial \bar{y}^2} \xi \right] \end{aligned} \tag{29}$$

It is noteworthy that the z -normal stress component, $\bar{\tau}_{zz}$, is implicitly involved in the momentum equations via the stress coefficient function. Substituting the above dimensionless stress components (Eqs. 20–24) into the combined form of the momentum equations in the x and y directions, Eq. (18) gives an explicit form of this equation with respect to the dimensionless stream function, which, together with nonslip at the walls and symmetry boundary conditions along the transverse axes, can be written as follows:

$$\begin{cases} C_1 \frac{\partial \bar{\varphi}}{\partial \bar{x}} + C_2 \frac{\partial \bar{\varphi}}{\partial \bar{y}} + C_3 \frac{\partial^2 \bar{\varphi}}{\partial \bar{x}^2} + C_4 \frac{\partial^2 \bar{\varphi}}{\partial \bar{y}^2} + C_5 \frac{\partial^2 \bar{\varphi}}{\partial \bar{x} \partial \bar{y}} + C_6 \frac{\partial^4 \bar{\varphi}}{\partial \bar{x}^4} + C_7 \frac{\partial^4 \bar{\varphi}}{\partial \bar{y}^4} \\ \quad + C_8 \frac{\partial^4 \bar{\varphi}}{\partial \bar{x}^2 \partial \bar{y}^2} + C_9 \frac{\partial^4 \bar{\varphi}}{\partial \bar{x}^3 \partial \bar{y}} + C_{10} \frac{\partial^4 \bar{\varphi}}{\partial \bar{x} \partial \bar{y}^3} + C_{11} = 0 \quad (30) \\ \frac{\partial^2 \bar{\varphi}}{\partial \bar{x}^2} \Big|_{\bar{x}=0} = \frac{\partial^2 \bar{\varphi}}{\partial \bar{y}^2} \Big|_{\bar{y}=0} = 0, \quad \bar{\varphi}|_{\bar{x}=\alpha} = \bar{\varphi}|_{\bar{y}=1} = 0 \end{cases}$$

where C_i s are the dimensionless coefficients which are given in the “Appendix.” Similarly, the explicit form of the z -momentum equation in terms of axial velocity can be obtained by substituting the expressions equivalent to the dimensionless components of the stress tensor, $\bar{\tau}_{xz}$ and $\bar{\tau}_{yz}$, from Eqs. (23) and (24) into Eq. (19), and the final relation can be written as:

$$\begin{cases} F_1 \frac{\partial \bar{u}_z}{\partial \bar{x}} + F_2 \frac{\partial \bar{u}_z}{\partial \bar{y}} + F_3 \frac{\partial^2 \bar{u}_z}{\partial \bar{x}^2} + F_4 \frac{\partial^2 \bar{u}_z}{\partial \bar{y}^2} + F_5 \frac{\partial^2 \bar{u}_z}{\partial \bar{x} \partial \bar{y}} + F_6 = 0 \\ \frac{\partial \bar{u}_z}{\partial \bar{x}} \Big|_{\bar{x}=0} = \frac{\partial \bar{u}_z}{\partial \bar{y}} \Big|_{\bar{y}=0} = 0, \quad \bar{u}_z|_{\bar{x}=\alpha} = \bar{u}_z|_{\bar{y}=1} = 0 \quad (31) \end{cases}$$

in which, similar to Eq. (30), the nonslip at the walls and symmetry boundary conditions along the x - and y -axes is used for \bar{u}_z . Also, F_i s are the dimensionless coefficients which are given in the “Appendix.”

4 Computational method

In this section, the nonlinear system of equations consisting of the PB Eq. (10), the momentum Eqs. (30, 31) and the stress components extracted from constitutive equations of the PTT model (20–25) is numerically solved. The numerical method is based on the second-order central finite difference method which is used to replace the derivatives that

Table 1 Practical ranges of main operating parameters

Operating parameters	Values
Debye length (κ^{-1}) (Li 2004)	1–300 nm
Zeta potential (Karniadakis et al. 2006)	± 1 to ± 100 mV
Electric field (Karniadakis et al. 2006)	1–100 kV m^{-1}
Helmholtz–Smoluchowski velocity (u_{HS}) (Karniadakis et al. 2006)	10^{-4} –1 mms^{-1}
Half channel height (H) (Kandlikar et al. 2005)	1–100 μm
Half channel width (W)	1–10 H

appear in the aforementioned governing equations with their algebraic approximations. Then, the algebraic forms of the differential equations of electrical potential, axial velocity and stream function are rearranged in the following manner:

$$D_{\psi_p} \bar{\psi}_p = \sum_i D_{\psi_i} \bar{\psi}_{NB_i}; \quad D_{u_p} \bar{u}_p = \sum_i D_{u_i} \bar{u}_{NB_i} + D_{u_c};$$

$$D_{\varphi_p} \bar{\varphi}_p = \sum_i D_{\varphi_i} \bar{\varphi}_{NB_i} + D_{\varphi_c} \quad (32)$$

where D_{ψ} , D_u and D_{φ} are the coefficients obtained from the discretization of the related differential equations by FDM, and the subscripts p and NB refer to the central node and neighbor grid points in vertical and horizontal directions, respectively. The finite difference approximation of the stress tensor components is directly derived from Eqs. (20–25) in which the value of each component in the central node can be obtained from the discretized form of RHS of these equations, and consequently, their corresponding algebraic forms do not need any rearrangement. Afterward, the Gauss–Seidel iteration method is employed for solving the system of linear algebraic equations. Based on this iterative algorithm, we calculate the values of the dependent variables at the central grid points with index P by the latest computed values of these variables at the neighboring grid points (Hoffmann 1989). At first, the PB equation is separately computed to obtain $\bar{\psi}$ in the grid network, and then, the coupled momentum and PTT constitutive equations are solved in an iterative manner to obtain \bar{u}_z , $\bar{\tau}_{ij}$ and $\bar{\varphi}$. For the first loop, the calculation of variables starts with the initial guesses $\bar{\psi}^g = 0.1\bar{\psi}_0$, $\bar{u}_z^g = 0$, $\bar{\tau}_{ij}^g = 0$, and $\bar{\varphi}^g = 0$, together with the recently updated values on the RHS of Eq. (32), and the procedure for the subsequent iterations is continued until the specified overall relative error of 10^{-8} for the size of the velocity vector, $\|\bar{u}\| = \sqrt{\bar{u}_x^2 + \bar{u}_y^2 + \bar{u}_z^2}$, between two successive iterations is achieved.

5 Results and discussions

In this section, we discuss the influence of flow characteristics on secondary flow of the viscoelastic fluid in the rectangular cross section of microchannel. Since all the parameters ε , ξ and Wi_κ typically exhibit shear thinning, to reduce the number of the results, we keep the first two material parameters of the PTT fluid constant as $\varepsilon = 0.1$, $\xi = 0.005$ for all simulations except for the validation of numerical results, and by changing the Weissenberg number, we investigate the shear-thinning effect of viscoelastic fluids on the secondary flow in the presence of thick EDLs. Also, in conformity with the study of Park and Lee (2008a), we consider a symmetric monovalent electrolyte solution ($Z = 1$) at room temperature ($T_m = 298$ K). We also study the effect of various values of the Debye–Hückel parameter, channel aspect ratios and wall zeta potentials on the pattern, average and strength of the secondary viscoelastic flow in the next subsections. To do so, the ranges of electrokinetic and rheological parameters in the scope of practical microfluidic applications are given in Table 1. These data are used in selecting the values of the dimensionless factors for performing the parametric study.

5.1 Grid dependency check and method validation against 1D analytical model

Before a decision is to be made on the number of grids used for the viscoelastic flow simulation, a grid dependency study is conducted to ensure the independence of the solutions from further grid refinements. In order to quantify the amount of uncertainty arising from the grid size, we use the following flow quantities: (1) the average of primary flow in the half-width plane of the microchannel (i.e., $\bar{u}_z|_{\bar{x}=0} = \int_{-1}^1 \bar{u}_z(0, \bar{y}) d\bar{y}$) and (2) the average of secondary flow in the upper-right quadrant of cross-sectional plane of the microchannel (i.e., $SV_{ave} = \alpha^{-1} \int_0^1 \int_0^\alpha \sqrt{\bar{u}_x^2 + \bar{u}_y^2} d\bar{x}d\bar{y}$). Based on these two quantities, the results of grid dependency study are reported in Table 2.

As can be seen from Table 2, the number of the grids ($N_x \times N_y$) = (60 α \times 60) ascertains the minimum grid resolution required to obtain a grid-independent solution of both axial and secondary flows, and the denser grid network does not significantly change the accuracy of the numerical simulation. However, to improve the resolution of secondary flows at the cross-sectional plane of microchannel, we employ 150 α \times 150 grid points for all parametric studies, by which we can do more detailed investigations. Table 2

Table 2 Grid dependency study in $Re = 0.1$ and pure electroosmotic flow ($\Gamma = 0$)

Grid system (N_x, N_y)	Primary flow: $\tilde{u}_z _{\tilde{x}=0}$ ($\varepsilon = 0.1, \xi = 0, \alpha = 10, \tilde{\psi}_0 = 0.05, K = 10$)		Secondary flow: $SV_{ave} \times 10^{-6}$ ($\varepsilon = 0.1, \xi = 0.005, \alpha = 1, \tilde{\psi}_0 = 1, K = 10$)	
	$Wi_\kappa = 1$	$Wi_\kappa = 3$	$Wi_\kappa = 1$	$Wi_\kappa = 3$
$10\alpha \times 10$	1.8826425	2.6323484	1.3186936	6.6915638
$20\alpha \times 20$	1.9168937	2.9186377	2.4058636	10.4865657
$40\alpha \times 40$	1.9261405	2.9314147	2.5844364	12.0976186
$60\alpha \times 60$	1.9263063	2.9515068	2.6581452	12.1020496
$80\alpha \times 80$	1.9265754	2.9538102	2.6734153	12.1094756
$100\alpha \times 100$	1.9266942	2.9557021	2.6840230	12.1100002
Afonso et al. (2009)	1.9288888	2.9596000	–	–

also shows the comparison of $\tilde{u}_z|_{\tilde{x}=0}$ between the results of the analytical solution obtained by Afonso et al. (2009) and those of the present study. For this purpose, a large aspect ratio ($\alpha = 10$), low zeta potential ($\tilde{\psi}_0 = 0.05$) and zero second normal stress difference ($\xi = 0$) are used in the numerical simulation to meet the assumptions of the analytical solution. As can be seen, there is a negligible discrepancy between the results of these two works with respect to $\tilde{u}_z|_{\tilde{x}=0}$.

On the other hand, in order to qualitatively determine the difference between the numerical and analytical results along the y direction, the cross-sectional velocity profile at the half-depth plane, $\tilde{u}_z|_{\tilde{x}=0}$, obtained from these two methods is sketched in Fig. 2. As can be seen, for the typical values of $\Gamma = -2$ to 8, our results obtained from the numerical

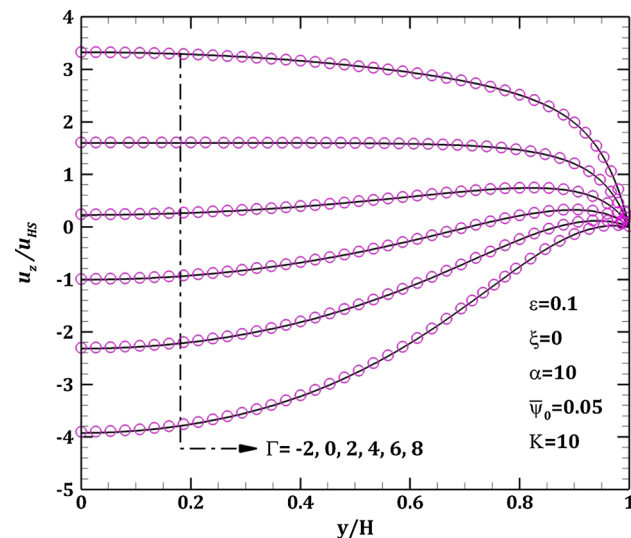


Fig. 2 Comparison between the results of the present numerical simulation (symbols) and the analytical solution (lines) obtained by Afonso et al. (2009)

simulation by FDM match the results of analytical solution very well, exhibiting an excellent accord again.

5.2 Comparison of FDM simulations with experimental data: secondary flow versus lateral particle migration

In this section, the results of the numerical method are compared with the experimental data pertinent to the lateral migration of particles suspended in a viscoelastic fluid. In the work of Lim et al. (2014), a polydimethylsiloxane (PDMS) microfluidic channel with $100 \times 50 \mu\text{m}$ width to height, i.e., the aspect ratio $\alpha = 2$, is utilized, and the non-Newtonian test fluid is 100 ppm aqueous polyacrylamide solution (PAA, Separan AP-273, $M_w = 5 \times 10^6$) with a total flow rate of $4.5 \mu\text{L}/\text{min}$ yielding a Reynolds number based on the hydraulic diameter and the mean velocity $Re_m \sim 0.476$. The measured values of the zero and infinite shear rate viscosities of the liquid are 12.36 and 1.96 mPa s, respectively. Based on these values and viscometric viscosity curve given in the experiment, we have fitted the rheological data of aqueous PAA solution to the PTT model, and the calculated material parameters are $\lambda = 0.58$, $\varepsilon = 9.7 \times 10^{-2}$ and $\xi = 1.73 \times 10^{-3}$ (Alves et al. 2001; Azaiez et al. 1996). As shown in Fig. 3a, the data are well fitted by the PTT model. Therefore, we use above material parameters for the test PTT polymeric liquid, and we compare the corresponding FDM results with experimental data.

Theoretically, the condition of pure pressure-driven flow in the experiment is provided only for the case of $|\Gamma| \rightarrow \infty$ (Afonso et al. 2009). Therefore, in order to obtain a flow regime similar to that in the experiment, high values of velocity scale ratios in the range of $-170 < \Gamma < -20$ are roughly used, such that, for a typical electroosmotic flow with $u_{HS} = 10^{-3} \text{ms}^{-1}$, the value of $\Gamma = -33.59$ corresponds to the flow rate of $4.5 \mu\text{L}/\text{min}$ given in the experiment. Also, by varying Γ from -20 to -170 , the total flow rate is changed, and correspondingly, Re_m increases from 0.19 to 4.91. In this step, a Weissenberg number based on

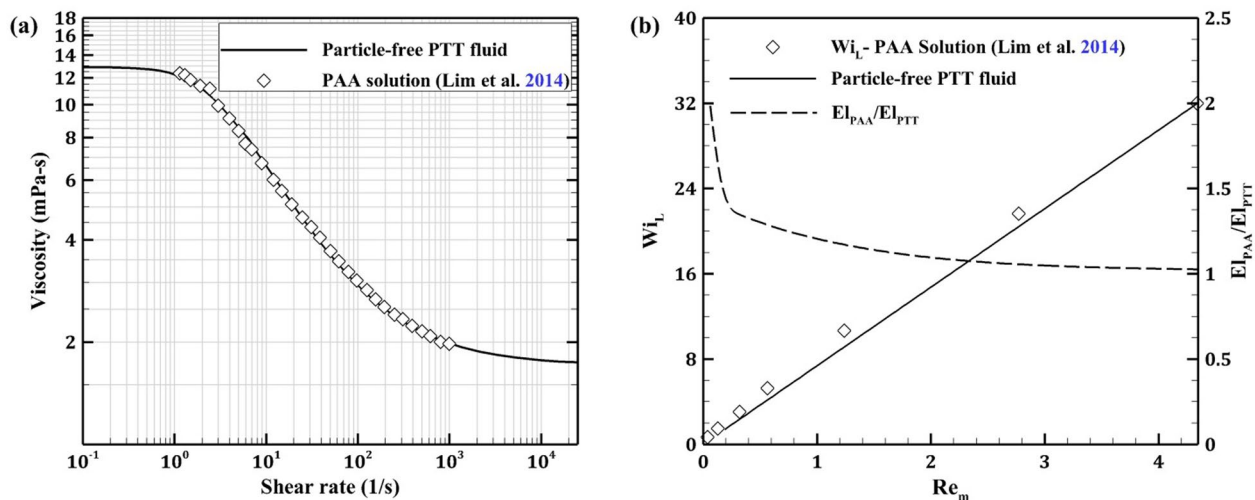


Fig. 3 **a** Variations of viscosity versus shear rate and **b** $Wi_L - Re_m - El_{PAA}/El_{PTT}$ diagram for PTT fluid (line) and 100 ppm aqueous PAA solution (symbols; Lim et al. 2014)

the axial channel length, L , and the mean velocity is defined (i.e., $Wi_L = \lambda u_m/L$), and by tuning the total flow rate via changing parameter Γ , the relationship between Wi_L and Re_m for the particle-free PTT fluid is investigated, and the results are compared with those of 100 ppm aqueous PAA solution containing 1- μm -diameter particles. It is noted that Wi_L in the experiment (i.e., Deborah number) is defined as the ratio of the relaxation time to a characteristic time equal to the duration of passage of particles through the main channel. As can be seen from Fig. 3b, there is a minimal discrepancy between the results of the PTT fluid and the experimental data of $Wi_L - Re_m$ which can be attributed to the retardation of microparticles relative to the suspending fluid flow.

Also, similar to the study of Lim et al. (2014), we define the elasticity number as $El = Wi_L/Re_m$ which provides a measure of the relative importance of elastic forces to inertial effects. The variations of the ratio of elasticity number for PAA solution containing 1- μm -diameter particles and that of particle-free PTT fluid, i.e., El_{PAA}/El_{PTT} , with respect to Re_m are also presented in Fig. 3b. As can be seen, at low values of Re_m , the ratio of El_{PAA}/El_{PTT} decreases rapidly and, then by further increasing the total flow rate, asymptotically approaches 1, which implies the fact that, at high values of Re_m , the elasticity number of both fluids reaches the same value regardless of the presence of microparticles in the liquid.

In order to demonstrate the importance of our numerical computations results for the cases of combined EO/PD flows, as a brief review, we first simulate the cross-streamlines of the PTT fluid in accordance with the conditions of the experiment (Lim et al. 2014), and then, we compare the simulated secondary flow pattern with the images of the

lateral migration of particles. Figure 4 presents the confocal cross-sectional images of the 1- μm -diameter particle displacements in upper-right quadrant of the microchannel at three distinct axial positions. The simulation result of the secondary flow pattern for $\alpha = 2$ and the aforementioned PTT material parameters is also depicted in this figure. As can be seen, the trajectories of the particles are influenced by the N_2 -induced secondary flow and approximately migrate toward the cross-streamlines pattern of the generated vortices. The plots qualitatively describe how the secondary flows arising from the transverse normal stress imbalance lead to a spiral trajectory of particles in the channel cross section. It is noteworthy that, as demonstrated in the previous investigations (Lim et al. 2014; Villone et al. 2013), by decreasing the size of the particles and, consequently, reducing the N_1 -elastic and inertial forces, the deviation of lateral particle trajectories from the streamlines of secondary flow is reduced and the role of N_2 -induced secondary flow in the lateral migration of sufficiently small particles is more pronounced.

5.3 Analysis of stream function and second normal stress difference

As discussed in Sect. 1, the nonzero second normal stress difference defined by $N_2 = \bar{\tau}_{xx} - \bar{\tau}_{yy}$ is considered as a prerequisite for the secondary flow motion of the PTT viscoelastic fluid through the straight microchannel with rectangular cross section. Figure 5 depicts the distribution of N_2 under parametric conditions $\alpha = 1$, $K = 10$, $\bar{\psi}_0 = 1$ and $Wi_K = 3$ at different values of velocity scale ratio, i.e., $\Gamma = -2$ to 8. As shown, for the cases of FPG, i.e., $\Gamma < 0$, the absolute value of N_2 at the regions near the walls

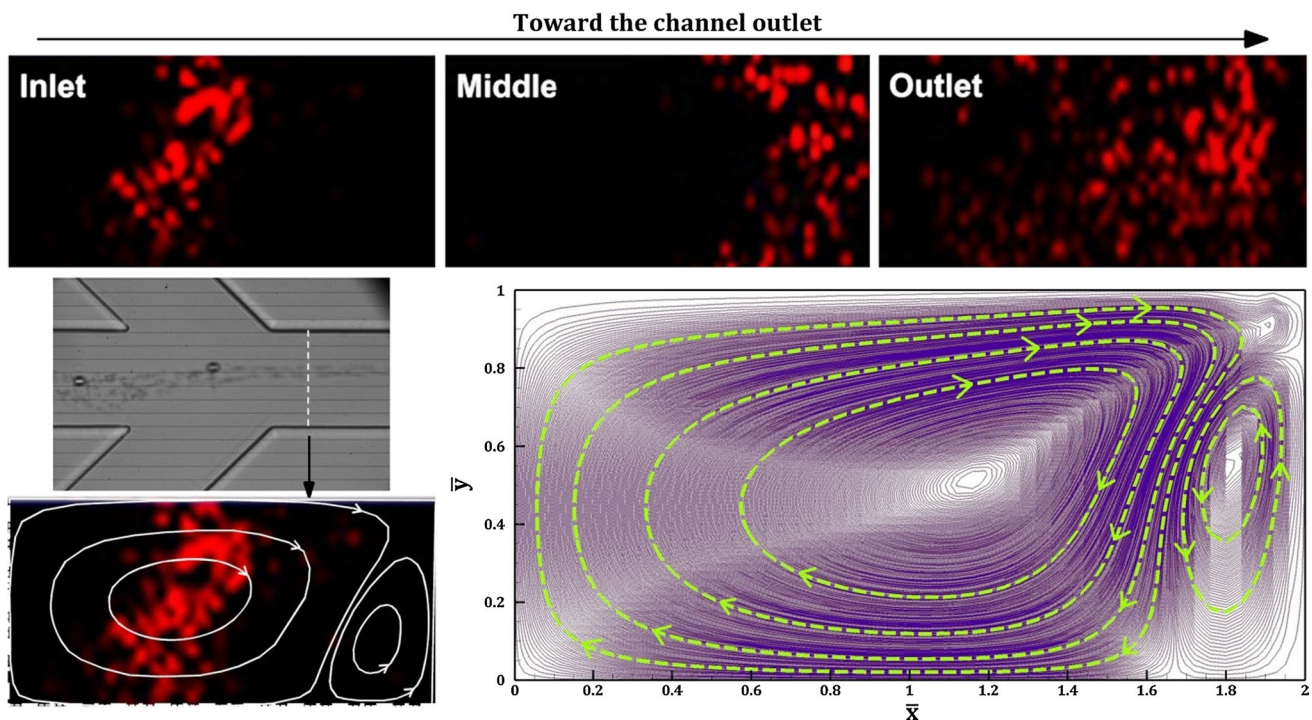


Fig. 4 The *bottom left figure*: FDM simulation of the N_2 -induced secondary flow in the conditions of the experiment. Other images: confocal images of the 1- μm particle displacements in *upper-right* quadrant

is larger than those at the corner and center of the channel cross section, so that, in the vast central region of the channel cross section, N_2 is almost equal to zero, while, for the cases of APG, i.e., $\Gamma > 0$, $|N_2|$ starts to increase in the regions far from the walls near the main diagonal of channel cross section. The reason is that the absolute value of second normal stress difference is proportional to the flow shear rate, and as can be seen from Fig. 2, the amount of shear rate in the middle regions of channel cross section increases with increasing the value of adverse pressure gradient. According to Fig. 5, the sign of N_2 changes across the main diagonal, possesses the negative value in the areas above the main diagonal and switches to the positive sign in the bottom half of the diagonal.

Based on the existence of nonzero second normal stress difference shown in Fig. 5, there is an opportunity for the development of the secondary flow. Also, due to the different contours of N_2 in the channel cross section, different patterns for the secondary velocity field, and consequently, various distributions of stream function at the channel cross section are to be expected. In this regard, the spatial distributions of $\bar{\varphi}$ for two values of $\Gamma = 4$ and -2 are sketched in Fig. 6a, b, respectively, under the conditions $\alpha = 1$, $K = 10$, $\bar{\psi}_0 = 1$ and $Wi_k = 3$. As can be seen from Fig. 6a, for the case of APG, the profile of $\bar{\varphi}$ exhibits four extrema in the upper-right quadrant of the channel cross section, while for

of the microchannel adapted from Lim et al. (2014) with permission from the corresponding author

the case of FPG, there are two extrema of $\bar{\varphi}$ in this region. Based on the definition of dimensionless vorticity function, at the regions with positive and negative values of $\bar{\varphi}$, the counterclockwise ($\bar{\omega} > 0$) and clockwise recirculation ($\bar{\omega} < 0$) emerge, respectively. Accordingly, we can approximate the strength of the vortices by measuring the absolute average value of the vorticity function at the region of each recirculating eddies. So, it can be seen from Fig. 6 that, due to the larger concavity, the two vortices in the case of FPG are stronger than all vortices in the case of APG. Also, as is evident from Fig. 6a, for the case of APG, the strength of the recirculating vortices decreases with increase in their distance from the corners of the microchannel.

5.4 Effect of different parameters on secondary flow pattern

The results of streamline projections for the conditions specified in Fig. 5a–f are shown in Fig. 7a–f, respectively. In the cases of zero and favorable pressure gradients, i.e., $\Gamma \leq 0$, a clockwise recirculation occurs in the region above the main diagonal of channel cross section, while a counterclockwise one prevails in the bottom half, such that the secondary flow goes from center of the solid walls to the corner and then inward to the center of the microchannel. The secondary flow pattern

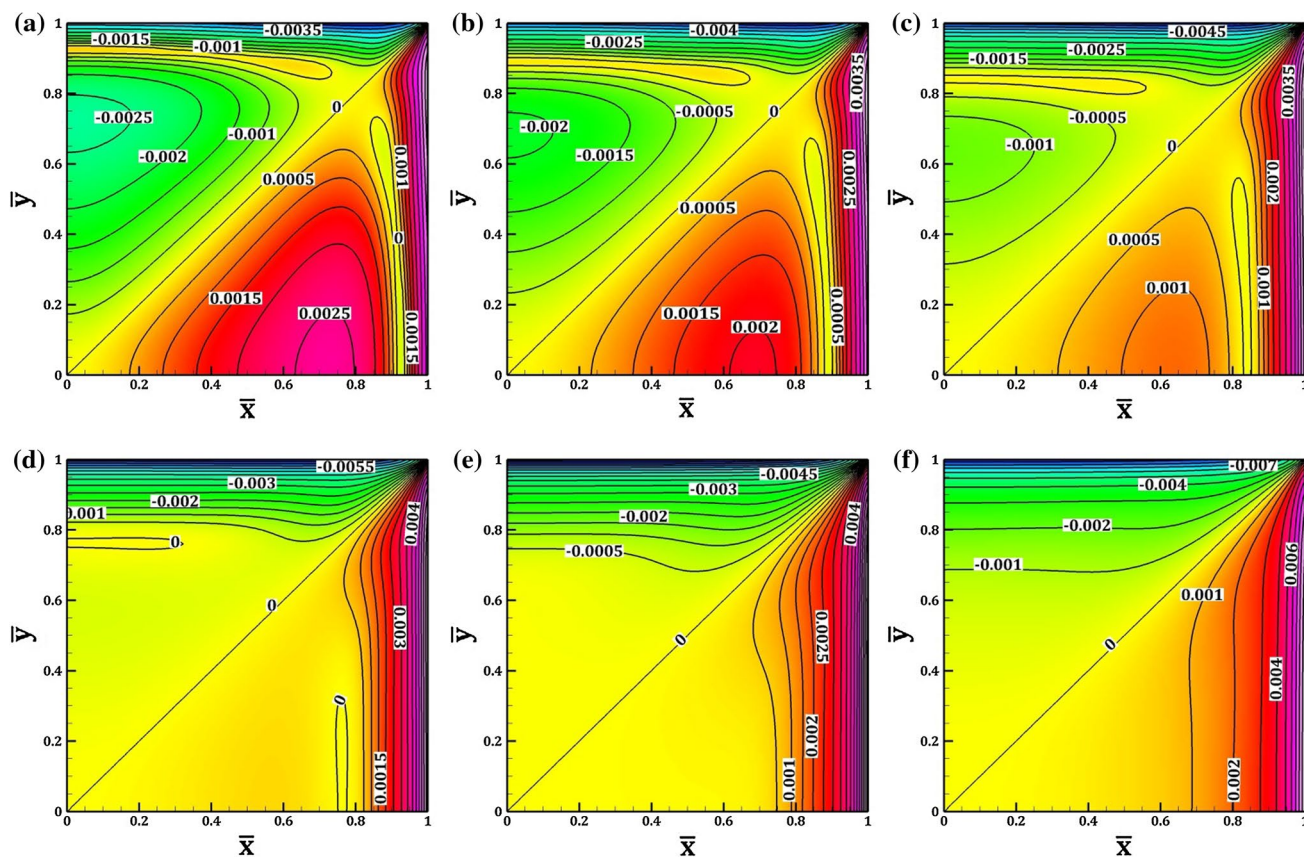


Fig. 5 Contours of second normal stress difference distribution at the *upper-right* quadrant of microchannel cross section for **a** $\Gamma = 8$, **b** $\Gamma = 6$, **c** $\Gamma = 4$, **d** $\Gamma = 2$, **e** $\Gamma = 0$ and **f** $\Gamma = -2$

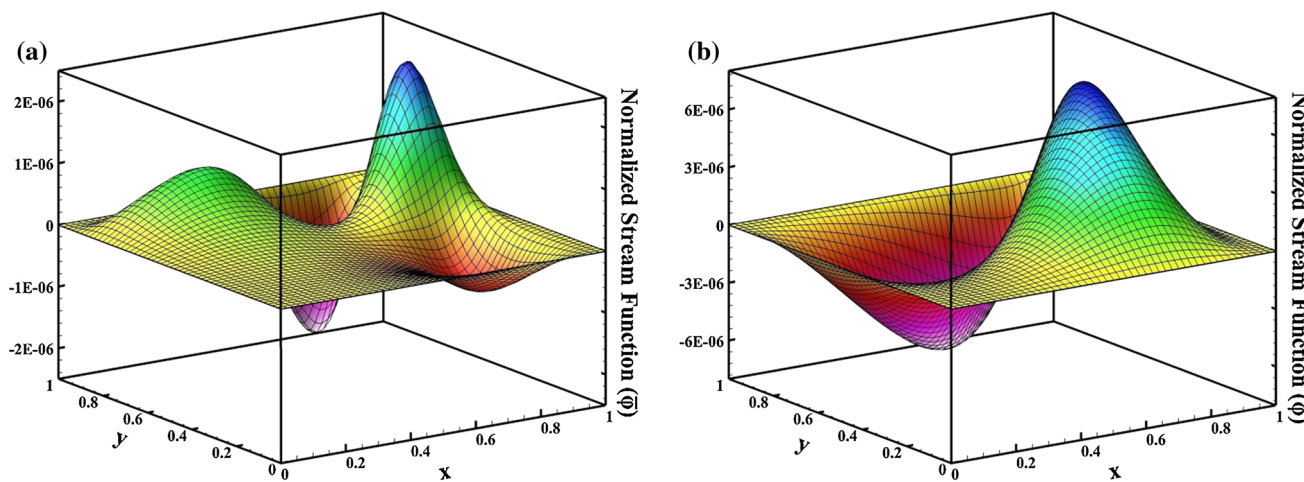


Fig. 6 Profiles of dimensionless stream function at the *upper-right* quadrant of the channel cross section for the cases of **a** $\Gamma = 4$ and **b** $\Gamma = -2$

for the case of FPG is qualitatively the same as that predicted by Park and Lee (2008a). However, for infinitesimal Debye lengths, the aforementioned study showed that the secondary flow approximately disappears in the absence of axial pressure gradient, while as can be seen

from Fig. 7e, in the presence of thick EDL, there are two large counter-rotating vortices at $\Gamma = 0$. In addition, for the cases of APG, one, two and four pairs of recirculating eddies emerge in $\Gamma = 2$, $\Gamma = 4$, and $\Gamma = 6, 8$, respectively, for which the direction of the secondary flow is

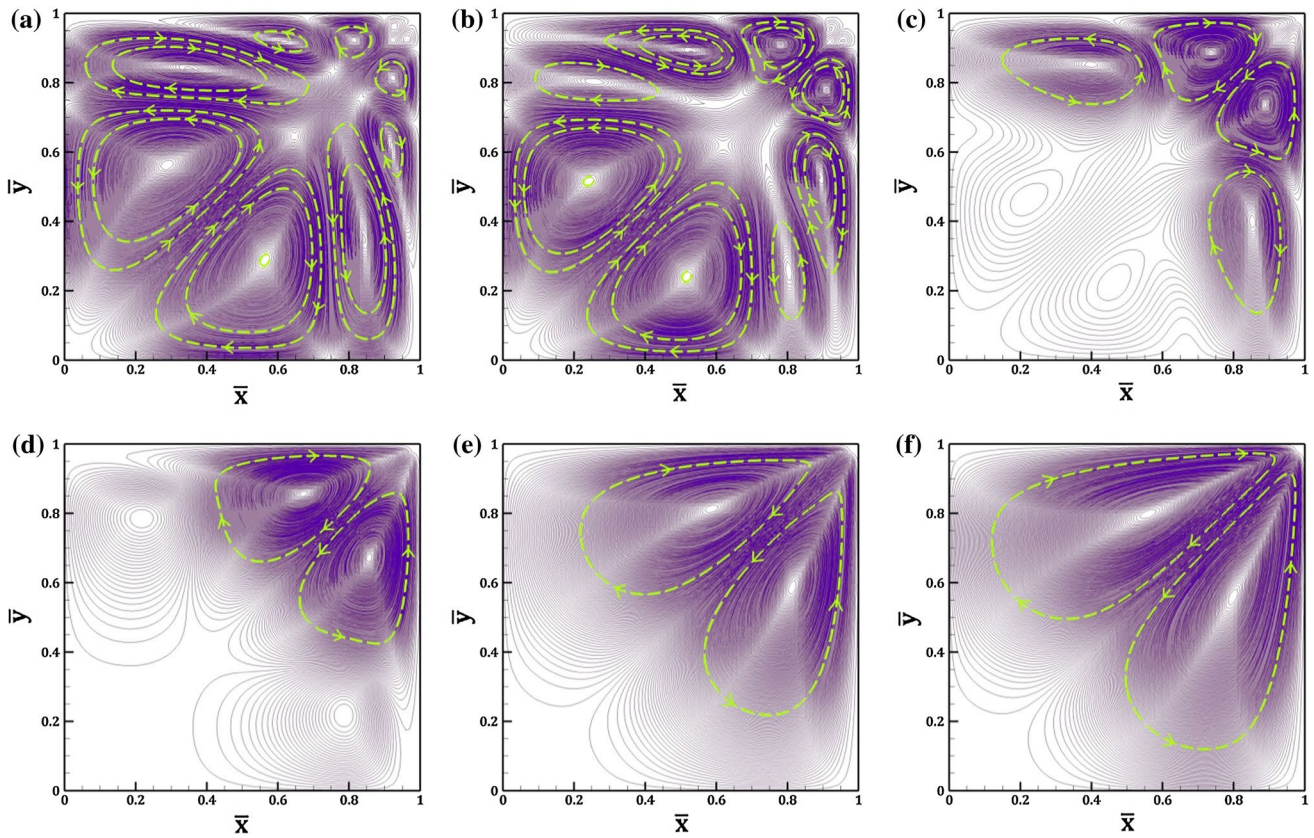


Fig. 7 Streamline projections for the conditions specified in Fig. 5; violet lines indicate the streamlines, and yellow lines denote the direction of recirculations

not straight from the center of the channel walls toward the corners.

It is expected that in the case of $\Gamma \rightarrow +\infty$ corresponding to the fully reverse pure PDF, a secondary flow with two recirculating eddies is retrieved (Hashemabadi and Etemad 2006; Park and Lee 2008a; Syrjälä 1998). Therefore, it can be concluded from Fig. 7 that, due to the presence of large Debye length, i.e., $K = 10$, a significant alteration occurs in the secondary flow pattern by transition from FPG to APG cases. Also, it can be seen from Fig. 7 that the extent of *dead fluid* zone in the central region of the channel cross section decreases with increase in the absolute value of velocity scale ratio.

Using accurate numerical model in a refined grid network, the present study is applicable to microchannels with various wall zeta potentials and arbitrary aspect ratios, and for electrolyte solutions with different Debye lengths. The effect of these parameters on the secondary flow pattern is investigated here which provides physical insight into the underlying secondary flow mechanism. As discussed above, in the presence of thick EDL, changing parameter Γ at a certain range leads to the alteration of the secondary flow from the pattern observed in previous study.

Figure 8a–c shows the effect of relative thickness of EDL, i.e., K , on the secondary flow pattern in a typical value of $\Gamma = 4$ corresponding to the case of APG, while the other parameters are set to $\alpha = 1$, $Wi_k = 3$, $\bar{\psi}_0 = 1$.

As can be seen from Fig. 8a, by increasing K from 10 to 20 and simultaneously decreasing the Debye length, the two recirculating eddies above the main diagonal join together retrieving again the previous secondary flow pattern demonstrated by Park and Lee (2008a). Also, the effect of $\bar{\psi}_0$ on the secondary flow pattern under the parametric conditions similar to those for Fig. 8a is depicted in Fig. 8b. From these contours, it is found that increasing $\bar{\psi}_0$ from 1 to 3 mostly affects the recirculating eddies near the corners, by which the pair of vortices in this regions are more stretched toward the corner.

All above computational results are obtained for the case of square channel cross section. At this stage, we investigate the effect of channel aspect ratio on the secondary flow pattern. Figure 9a–d shows the contours of streamline for two cases of APG and FPG through microchannels with different aspect ratios $\alpha = 1, 2$. When the shape of the channel cross section varies from square ($\alpha = 1$) to rectangle ($\alpha = 2$), the secondary flow exhibits different

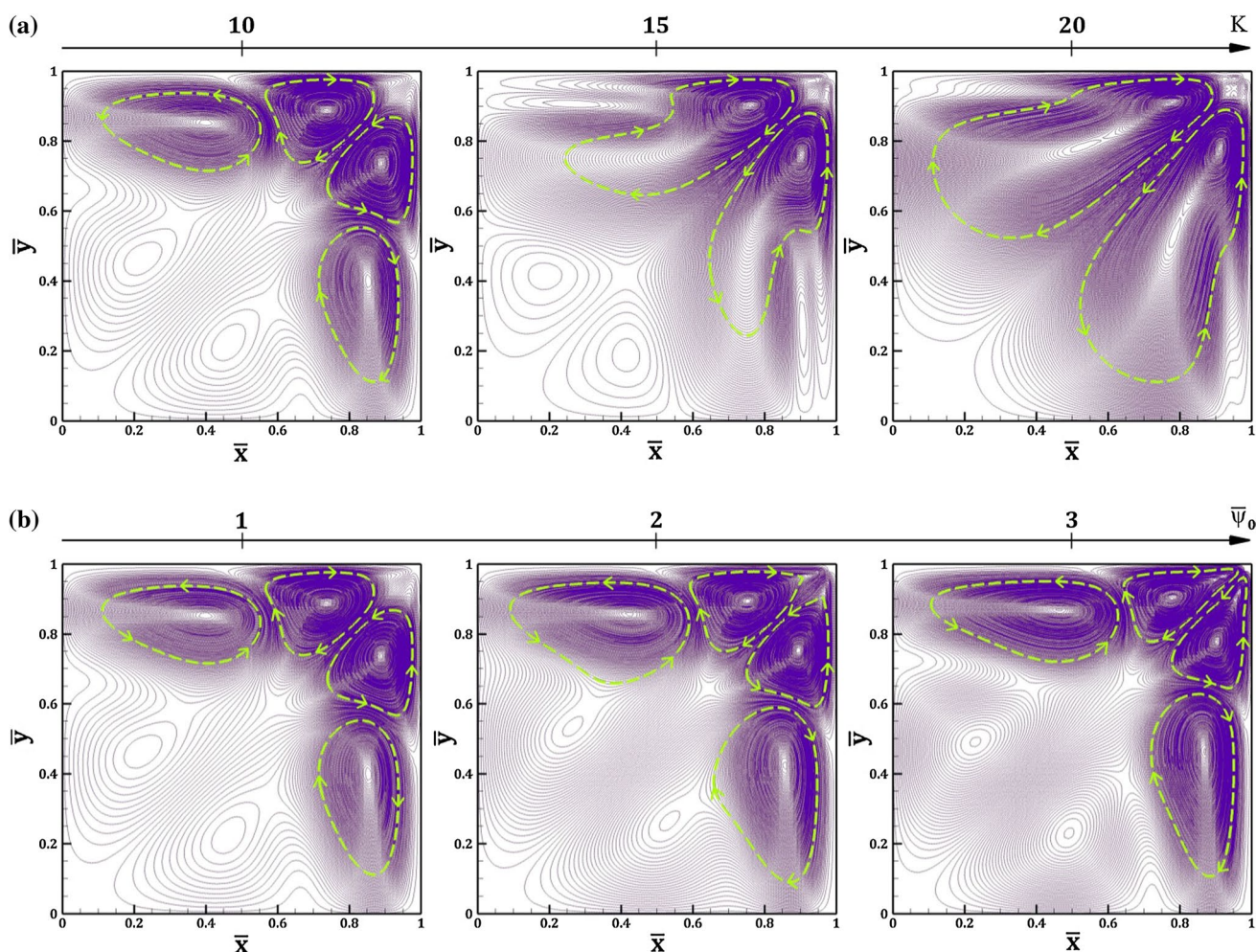


Fig. 8 Streamline projections for various **a** K and **b** $\bar{\psi}_0$; *violet lines* indicate the streamlines, and *yellow lines* denote the direction of recirculations

patterns for each case of Γ , so that, for the case of APG ($\Gamma = 4$), four recirculating eddies are transformed to the three eddies, as shown in Fig. 9a, b. For the case of FPG ($\Gamma = -2$) shown in Fig. 9c, d, increasing α from 1 to 2 does not change the number of eddies, but leads to an asymmetry between the two vortices with respect to the diagonal. Also in both cases of APG and FPG, as α increases, the size of eddies expands along the x direction.

5.5 Effect of different parameters on the strength and average of secondary flow

In addition to the average of secondary flow velocity defined in Sect. 4, we introduce another quantity termed the strength of secondary flow as $SV_m = \max \left\{ \sqrt{\bar{u}_x^2 + \bar{u}_y^2} \right\}_\Pi$ in which Π is the whole area of the channel cross section (Hashemabadi and Etemad 2006; Park and Lee 2008a;

Poole et al. 2013). SV_m gives another tool to quantitatively determine the magnitude of the secondary flow, while SV_{ave} provides an information about the extent of dispersion of the secondary flow throughout the channel cross section. Figure 10 plots the strength and average of secondary flow against velocity scale ratio in the range of $-6 \leq \Gamma \leq 6$ for various values of the Weissenberg number (sections a, e), dimensionless Debye–Hückel parameter (sections b, f), dimensionless wall zeta potential (sections c, g) and channel aspect ratio (sections d, h). The symbols in the plots of Fig. 10 represent the values directly obtained from the present numerical simulation.

In addition, to quantitatively study the functionality of SV_m and SV_{ave} with respect to Γ in various parametric conditions and to provide theoretically useful results, a fourth-order polynomial curve fitting of the symbols is performed, and the related coefficients are provided in Table 3. It is noted that, in all figures, the black solid lines with triangle

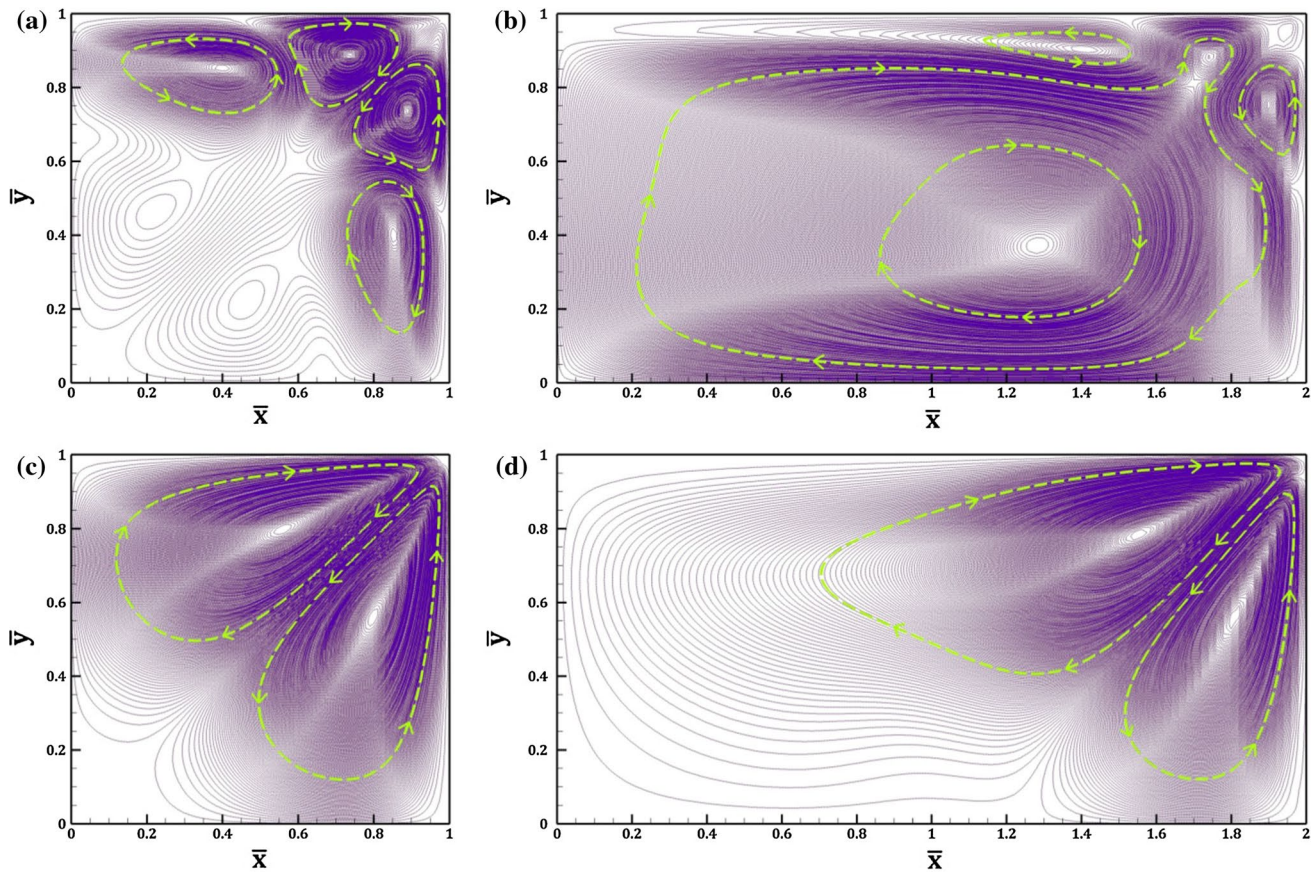


Fig. 9 Streamline projections at two channel aspect ratios in the cases of **a, b** APG ($\Gamma = 4$) and **c, d** FPG ($\Gamma = -2$); violet lines indicate the streamlines, and yellow lines denote the direction of recirculations

symbols are in the same parametric conditions. According to the statistical calculations, for all curves, R^2 is greater than 97 % which indicates the goodness of the polynomial curve fittings in modeling the variations of SV_m and SV_{ave} with respect to $\Gamma \in (-6, 6)$.

As can be seen from all plots of Fig. 10a–h, the sensitivity of SV_m and SV_{ave} with respect to the electrokinetic and geometrical parameters decreases by decreasing the absolute value of Γ . However, as shown in Fig. 10a, e, by increasing the Weissenberg number, the strength and average of secondary flow increases monotonically in all values of velocity scale ratio. It can be seen from Fig. 10b, f that at large negative values of Γ , as K increases from 10 to 20, the strength and average of secondary flow drops by approximately an order of magnitude, which implies that SV_m strongly depends on the thickness of the EDL.

As the value of SV_m approaches to SV_{ave} , the distribution of secondary flow is more uniform throughout the cross-sectional area of microchannel. On the other hand, all plots of Fig. 10 at $\alpha=1$ denote that, for FPG cases, the rate of change of SV_m with respect to Γ beyond its extremum value is in the order of 10^{-4} , while the rate of

this change for SV_{ave} is $\sim 10^{-5}$. So, we can conclude that the maximum uniformity of the secondary flow occurs at the extremum values of SV_{ave} and SV_m in which both the extremum points are located at approximately the same Γ . In this regard, Fig. 10b, f shows that these minimum values of SV_m and SV_{ave} decrease as K increases, and the related extremum points go toward the larger negative values of Γ . According to these observations, the prior conclusion done by Park and Lee (2008a), which expressed that the larger external pressure gradients, i.e., larger $|\Gamma|$, result in a stronger secondary flow, is only true for the cases of very thin EDLs, such that, in the case of $K = 20$ shown in Fig. 10b, SV_m decreases at $\Gamma : 4 \rightarrow -2$ and then increases at $\Gamma : -2 \rightarrow -6$.

As depicted in Fig. 10c, g, increasing $\bar{\psi}_0$ from 1 to 3 does not significantly change the plots of $SV_m - \Gamma$ and $SV_{ave} - \Gamma$ which are previously demonstrated by streamline contours of secondary flow shown in Fig. 8b. However, as shown in Fig. 10d, h, the effect of channel aspect ratio on SV_m and SV_{ave} is more dramatic. It can be observed that there is a non-monotonic change in the strength and average of secondary flow with respect to α for the cases

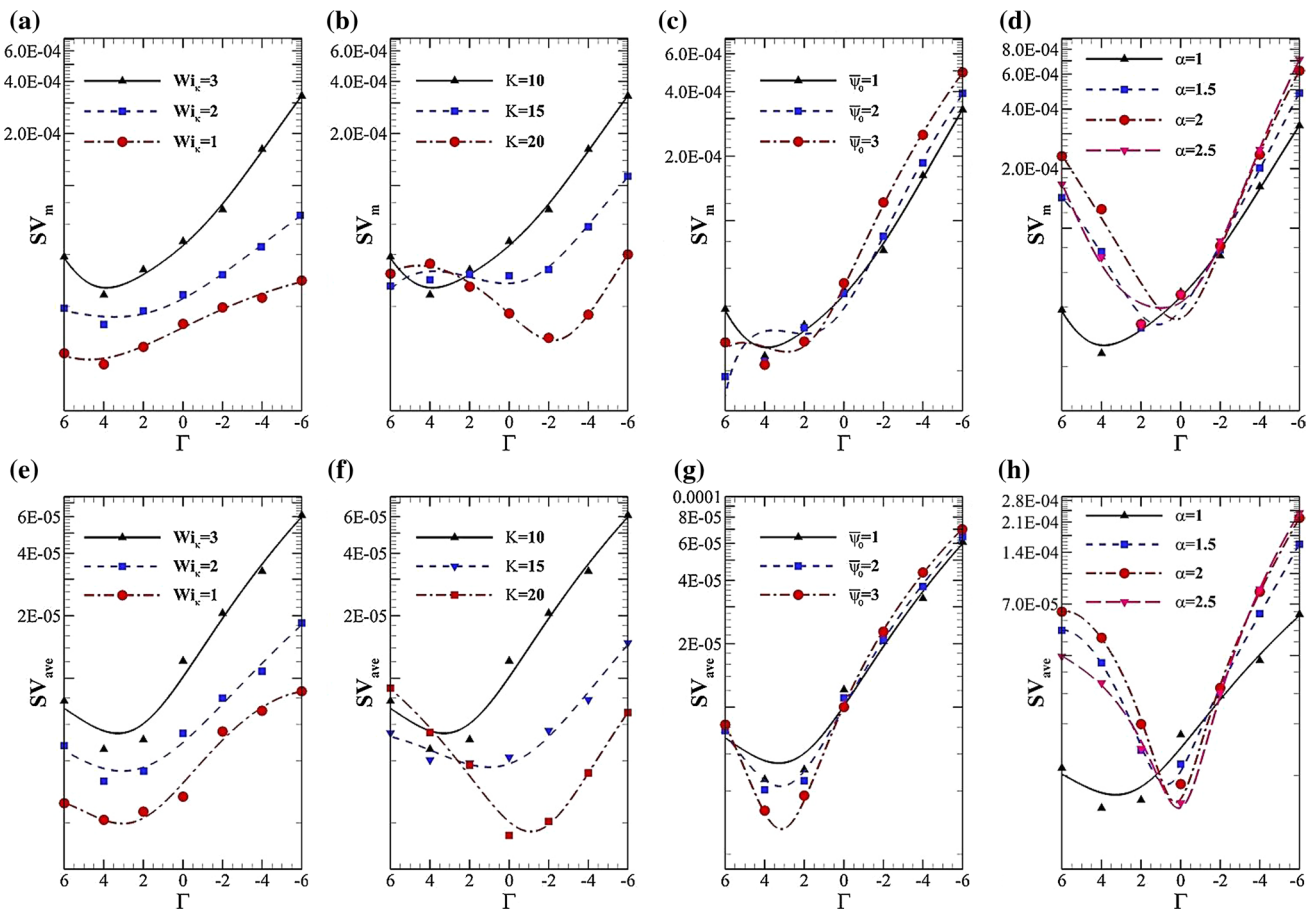


Fig. 10 Variations of SV_m and SV_{ave} with respect to Γ in various **a, e** Wi_k at $K = 10, \alpha = 1, \bar{\psi}_0 = 1$, **b, f** K at $Wi_k = 3, \alpha = 1, \bar{\psi}_0 = 1$, **c, g** $\bar{\psi}_0$ at $Wi_k = 3, K = 10, \alpha = 1$, and **d, h** α at $Wi_k = 3, K = 10, \bar{\psi}_0 = 1$

of APG and zero pressure gradients, such that, by increasing α from 1 to 2, both SV_m and SV_{ave} increase in all values of $\Gamma \geq 0$ and then decrease with increasing α from 2 to 2.5, while we can see that, for the case of FPG, SV_m and SV_{ave} monotonically increase with increasing α in all values of $\Gamma < 0$. Also, alterations in SV_m and SV_{ave} due to the change in channel aspect ratio are more prominent at low range of $1 \lesssim \alpha \lesssim 2$ and, then, tend to saturate at the higher ranges. For the sake of clarity of figure, we excluded the results for $\alpha > 2.5$, in which a significant change in SV_m and SV_{ave} due to varying α was not observed.

6 Conclusions

We presented a numerical simulation on viscoelastic secondary flows through rectangular microchannels under the combined effect of electroosmosis and hydrodynamics. The viscoelastic fluid rheologically obeys the complete form of PTT model with the Gordon–Schowalter convected derivative of the stress tensor and linearized stress coefficient function

which covers the constitutive equations of the UCM, Johnson–Segalman and FENE-P models. In order to numerically solve the governing equations, we employed the second-order central FDM in very refined grid network. The validation of our numerical scheme against the analytical solution from literature revealed the excellent accuracy of the present analysis with negligible error. In order to demonstrate the importance and applicability of our investigation, we then compared the results of our numerical method against the experimental data extracted from the literature, and we investigated the influential role of secondary flows in lateral migration of microparticles suspended in a viscoelastic fluid.

We illustrated the distribution of the second normal stress difference as well as the pattern, strength and average of secondary flow under different electrokinetic and rheological parameters, and various channel aspect ratios, which provides a clear understanding on the contribution of each operating parameter to the formation of recirculating eddies at the channel cross section. To the best of our knowledge, it is the first study which comprehensively investigates the effect of all aforementioned parameters on

Table 3 Coefficients of polynomial curve fitting for SV_m and SV_{ave} with respect to Γ

		$SV_m = a_0 + a_1\Gamma + a_2\Gamma^2 + a_3\Gamma^3 + a_4\Gamma^4, \quad SV_{ave} = b_0 + b_1\Gamma + b_2\Gamma^2 + b_3\Gamma^3 + b_4\Gamma^4$					R^2
		a_0 b_0	a_1 b_1	a_2 b_2	a_3 b_3	a_4 b_4	
Sec. a, e	$Wi_k = 1$	1.512e-5	-1.924e-6	1.105e-7	1.307e-8	0	0.986953
		3.123e-6	-7.565e-7	1.181e-7	6.920e-9	-1.409e-9	0.983042
	$Wi_k = 2$	2.222e-5	-3.089e-6	5.854e-7	-2.704e-8	0	0.990302
		4.901e-6	-9.244e-7	1.772e-7	-5.807e-9	0	0.981817
	$Wi_k = 3$	4.503e-5	-1.039e-5	2.199e-6	-3.880e-7	4.635e-8	0.996637
		1.013e-5	-3.216e-6	6.501e-7	-3.286e-8	0	0.982185
Sec. b, f	$K = 15$	2.722e-5	-3.248e-7	1.148e-6	-1.930e-7	0	0.983828
		3.865e-6	-2.957e-7	1.668e-7	-1.331e-8	0	0.979062
	$K = 20$	1.817e-5	4.194e-6	4.884e-7	-1.368e-7	0	0.994899
		2.029e-6	3.748e-7	1.620e-7	-5.659e-9	0	0.982786
Sec. c, g	$\tilde{\psi}_0 = 2$	3.901e-5	-1.156e-5	4.547e-6	-5.466e-7	0	0.982439
		1.002e-5	-3.862e-6	7.159e-7	-2.386e-8	0	0.995862
	$\tilde{\psi}_0 = 3$	4.926e-5	-2.124e-5	5.786e-6	-4.857e-7	0	0.996081
		1.017e-5	-4.864e-6	8.128e-7	-8.882e-9	0	0.999656
Sec. d, h	$\alpha = 1.5$	3.877e-5	-1.085e-5	4.943e-6	-1.532e-7	7.382e-8	0.991588
		7.424e-6	-3.327e-6	2.264e-6	8.173e-8	1.059e-8	0.998301
	$\alpha = 2$	3.511e-5	-3.131e-6	7.211e-6	-8.142e-7	1.034e-7	0.979024
		5.130e-6	-1.747e-6	3.482e-6	-8.436e-8	9.161e-9	0.995854
	$\alpha = 2.5$	4.229e-5	-6.121e-6	4.358e-6	-1.081e-6	1.846e-7	0.991247
		4.554e-6	-5.241e-7	2.713e-6	-4.544e-7	2.619e-8	0.998740

secondary flows of PTT fluids through rectangular microchannels in the presence of both EO and pressure driving forces. The significant findings and insights obtained from this study include:

- Based on different distribution of second normal stress difference at the channel cross section in the presence of zero, adverse and favorable pressure gradients, various secondary flow patterns were observed for these cases. In the cases of zero and FPGs, a pair of recirculating eddies occur across the main diagonal of channel cross section. However, for the cases of APGs, more than one pair of recirculating eddies emerges in various values of Γ demonstrating a significant alteration in the secondary flows pattern by transition from FPG to APG cases in the presence of thick EDLs.
- Comparing to the prior studies, at low values of the Debye–Hückel parameter, there is a significant deviation of the pattern of secondary flows throughout the channel cross section, especially in the case of APG. Also, the main effect of wall zeta potential is on the recirculating vortices located at the corners of microchannel. In addition, when the shape of the channel cross section varies from square to rectangle, the number of vortices decreases in the case of APG, while in the case of FPG, the increase in the channel aspect ratio only leads to the change in the shape of the recirculating eddies.
- It was observed that the sensitivity of SV_m and SV_{ave} with respect to electrokinetic and geometrical parameters decreases by decreasing the absolute value of Γ . With increase in the Weissenberg number, the strength and average of secondary flows increases monotonically in all values of velocity scale ratio. At large negative values of Γ , as K increases, the strength and average of secondary flows drops by approximately an order of magnitude. Increasing dimensionless zeta potential does not significantly change SV_m and SV_{ave} , while alterations in these quantities, due to the change in channel aspect ratio, are more prominent at low range of $1 \lesssim \alpha \lesssim 2$ and, then, tend to saturate at higher values of α .

Acknowledgments The use of a high-speed computer is indispensable in connection with performing the present numerical analysis. Our computations were performed by HPC Center of Sharif University of Technology which is gratefully acknowledged.

Appendix

- The coefficients C_i s in Eq. (30) are given as:

$$C_1 = -\text{Re} \frac{\partial \bar{\Omega}}{\partial \bar{y}}, \quad C_2 = \text{Re} \frac{\partial \bar{\Omega}}{\partial \bar{x}} \tag{33}$$

$$C_3 = \left[1 - \frac{Wi_k}{2K} (\xi \bar{\tau}_{yy} + (\xi - 2)\bar{\tau}_{xx}) \right] \left[\frac{\partial^2 \Lambda_3}{\partial \bar{x}^2} - \frac{\partial^2 \Lambda_3}{\partial \bar{y}^2} \right] + \frac{Wi_k}{K} \left\{ \frac{\partial^2 \bar{\tau}_{yx}}{\partial \bar{x} \partial \bar{y}} (\xi \Lambda_1 + (2 - \xi)\Lambda_2) + \bar{\tau}_{xy} \left[\xi \frac{\partial^2 \Lambda_1}{\partial \bar{x} \partial \bar{y}} + (2 - \xi) \frac{\partial^2 \Lambda_2}{\partial \bar{x} \partial \bar{y}} \right] + \frac{\Lambda_3}{2} \left[\xi \frac{\partial^2 \bar{\tau}_{yy}}{\partial \bar{y}^2} + (2 - \xi) \frac{\partial^2 \bar{\tau}_{xx}}{\partial \bar{x}^2} \right] - \frac{\Lambda_3}{2} \left[\xi \frac{\partial^2 \bar{\tau}_{yy}}{\partial \bar{x}^2} + (2 - \xi) \frac{\partial^2 \bar{\tau}_{xx}}{\partial \bar{y}^2} \right] \right\} \quad (34)$$

$$C_4 = \left[1 - \frac{Wi_k}{2K} (\xi \bar{\tau}_{xx} + (\xi - 2)\bar{\tau}_{yy}) \right] \left[\frac{\partial^2 \Lambda_3}{\partial \bar{y}^2} - \frac{\partial^2 \Lambda_3}{\partial \bar{x}^2} \right] + \frac{Wi_k}{K} \left\{ \frac{\partial^2 \bar{\tau}_{yx}}{\partial \bar{x} \partial \bar{y}} (\xi \Lambda_2 + (2 - \xi)\Lambda_1) + \bar{\tau}_{xy} \left[\xi \frac{\partial^2 \Lambda_2}{\partial \bar{x} \partial \bar{y}} + (2 - \xi) \frac{\partial^2 \Lambda_1}{\partial \bar{x} \partial \bar{y}} \right] + \frac{\Lambda_3}{2} \left[\xi \frac{\partial^2 \bar{\tau}_{xx}}{\partial \bar{x}^2} + (2 - \xi) \frac{\partial^2 \bar{\tau}_{yy}}{\partial \bar{y}^2} \right] - \frac{\Lambda_3}{2} \left[\xi \frac{\partial^2 \bar{\tau}_{xx}}{\partial \bar{y}^2} + (2 - \xi) \frac{\partial^2 \bar{\tau}_{yy}}{\partial \bar{x}^2} \right] \right\} \quad (35)$$

$$C_5 = 2 \frac{\partial^2 \Lambda_1}{\partial \bar{x} \partial \bar{y}} + 2 \frac{\partial^2 \Lambda_2}{\partial \bar{x} \partial \bar{y}} \quad (36)$$

$$C_6 = \left[1 - \frac{Wi_k}{2K} (\xi \bar{\tau}_{yy} + (\xi - 2)\bar{\tau}_{xx}) \right] \Lambda_3 \quad (37)$$

$$C_7 = \left[1 - \frac{Wi_k}{2K} (\xi \bar{\tau}_{xx} + (\xi - 2)\bar{\tau}_{yy}) \right] \Lambda_3 \quad (38)$$

$$C_8 = 2(\Lambda_1 + \Lambda_2) - 2 \left[1 - \frac{Wi_k}{2K} (\bar{\tau}_{xx} + \bar{\tau}_{yy})(\xi - 1) \right] \Lambda_3 \quad (39)$$

$$C_9 = \frac{Wi_k}{K} \bar{\tau}_{xy} (\xi \Lambda_1 + (2 - \xi)\Lambda_2) \quad (40)$$

$$C_{10} = \frac{Wi_k}{K} \bar{\tau}_{xy} (\xi \Lambda_2 + (2 - \xi)\Lambda_1) \quad (41)$$

$$C_{11} = \frac{\partial^2 I_1}{\partial \bar{x} \partial \bar{y}} - \frac{\partial^2 I_2}{\partial \bar{x} \partial \bar{y}} - \frac{\partial^2 I_3}{\partial \bar{y}^2} + \frac{\partial^2 I_3}{\partial \bar{x}^2} \quad (42)$$

• The coefficients F_i s in Eq. (31) are given as:

$$F_1 = -Re \frac{\partial \bar{\varphi}}{\partial \bar{y}} + \frac{Wi_k}{2K} \left[\Lambda_4 \left(\frac{\partial \bar{\tau}_{xx}}{\partial \bar{x}} (2 - \xi) - \frac{\partial \bar{\tau}_{zz}}{\partial \bar{x}} \xi \right) + \frac{\partial \Lambda_5}{\partial \bar{y}} \bar{\tau}_{xy} (2 - \xi) + \Lambda_5 \frac{\partial \bar{\tau}_{xy}}{\partial \bar{y}} (2 - \xi) \right] + \frac{\partial \Lambda_4}{\partial \bar{x}} \left[1 - \frac{Wi_k}{2K} (\bar{\tau}_{xx}(\xi - 2) + \bar{\tau}_{zz}\xi) \right] \quad (43)$$

$$F_2 = Re \frac{\partial \bar{\varphi}}{\partial \bar{x}} + \frac{Wi_k}{2K} \left[\Lambda_5 \left(\frac{\partial \bar{\tau}_{yy}}{\partial \bar{y}} (2 - \xi) - \frac{\partial \bar{\tau}_{zz}}{\partial \bar{y}} \xi \right) + \frac{\partial \Lambda_4}{\partial \bar{x}} \bar{\tau}_{xy} (2 - \xi) + \Lambda_4 \frac{\partial \bar{\tau}_{xy}}{\partial \bar{x}} (2 - \xi) \right] + \frac{\partial \Lambda_5}{\partial \bar{y}} \left[1 - \frac{Wi_k}{2K} (\bar{\tau}_{yy}(\xi - 2) + \bar{\tau}_{zz}\xi) \right] \quad (44)$$

$$F_3 = \Lambda_4 \left[1 - \frac{Wi_k}{2K} (\bar{\tau}_{xx}(\xi - 2) + \bar{\tau}_{zz}\xi) \right] \quad (45)$$

$$F_4 = \Lambda_5 \left[1 - \frac{Wi_k}{2K} (\bar{\tau}_{yy}(\xi - 2) + \bar{\tau}_{zz}\xi) \right] \quad (46)$$

$$F_5 = \frac{Wi_k}{2K} \bar{\tau}_{xy} (2 - \xi) (\Lambda_4 + \Lambda_5) \quad (47)$$

$$F_6 = -\Gamma + \frac{\partial I_4}{\partial \bar{x}} + \frac{\partial I_5}{\partial \bar{y}} + \frac{K^2}{\bar{\psi}_0} \sinh \bar{\psi} \quad (48)$$

References

Afonso A, Alves M, Pinho F (2009) Analytical solution of mixed electro-osmotic/pressure driven flows of viscoelastic fluids in microchannels. *J Non-Newtonian Fluid Mech* 159:50–63

Afonso A, Alves M, Pinho F (2011) Electro-osmotic flow of viscoelastic fluids in microchannels under asymmetric zeta potentials. *J Eng Math* 71:15–30

Afonso A, Ferrás L, Nóbrega J, Alves M, Pinho F (2014) Pressure-driven electrokinetic slip flows of viscoelastic fluids in hydrophobic microchannels. *Microfluid Nanofluid* 16:1131–1142

Alves MA, Pinho FT, Oliveira PJ (2001) Study of steady pipe and channel flows of a single-mode Phan-Thien–Tanner fluid. *J Non-Newtonian Fluid Mech* 101:55–76

Azaiez J, Guenette R, Ait-Kadi A (1996) Numerical simulation of viscoelastic flows through a planar contraction. *J Non-Newtonian Fluid Mech* 62:253–277

Babaie A, Sadeghi A, Saidi MH (2011) Combined electroosmotically and pressure driven flow of power-law fluids in a slit microchannel. *J Non-Newtonian Fluid Mech* 166:792–798

Babaie A, Saidi MH, Sadeghi A (2012) Electroosmotic flow of power-law fluids with temperature dependent properties. *J Non-Newtonian Fluid Mech* 185:49–57

- Berli CL (2010) Output pressure and efficiency of electrokinetic pumping of non-Newtonian fluids. *Microfluid Nanofluid* 8:197–207
- Bhagat AAS, Kuntaegowdanahalli SS, Papautsky I (2008) Continuous particle separation in spiral microchannels using dean flows and differential migration. *Lab Chip* 8:1906–1914
- Bilitewski U, Genrich M, Kadow S, Mersal G (2003) Biochemical analysis with microfluidic systems. *Anal Bioanal Chem* 377:556–569
- Bodnár T, Sequeira A, Prosi M (2011) On the shear-thinning and viscoelastic effects of blood flow under various flow rates. *Appl Math Comput* 217:5055–5067
- Brust M, Schaefer C, Doerr R, Pan L, Garcia M, Arratia P, Wagner C (2013) Rheology of human blood plasma: viscoelastic versus Newtonian behavior. *Phys Rev Lett* 110:078305
- Chatterjee A (2011) Size-dependant separation of multiple particles in spiral microchannels. University of Cincinnati
- Chow AW (2002) Lab-on-a-chip: opportunities for chemical engineering. *AIChE J* 48:1590–1595
- Chung AJ, Gossett DR, Di Carlo D (2013) Three dimensional, sheathless, and high-throughput microparticle inertial focusing through geometry-induced secondary flows. *Small* 9:685–690
- Cruz D, Pinho F, Oliveira P (2005) Analytical solutions for fully developed laminar flow of some viscoelastic liquids with a Newtonian solvent contribution. *J Non-Newtonian Fluid Mech* 132:28–35
- D'Avino G, Romeo G, Villone MM, Greco F, Netti PA, Maffettone PL (2012) Single line particle focusing induced by viscoelasticity of the suspending liquid: theory, experiments and simulations to design a micropipe flow-focuser. *Lab Chip* 12:1638–1645
- Debbaut B, Dooley J (1999) Secondary motions in straight and tapered channels: experiments and three-dimensional finite element simulation with a multimode differential viscoelastic model. *J Rheol* 43:1525–1545
- Debbaut B, Avalosse T, Dooley J, Hughes K (1997) On the development of secondary motions in straight channels induced by the second normal stress difference: experiments and simulations. *J Non-Newtonian Fluid Mech* 69:255–271
- Dhinakaran S, Afonso A, Alves M, Pinho F (2010) Steady viscoelastic fluid flow between parallel plates under electro-osmotic forces: Phan-Thien–Tanner model. *J Colloid Interface Sci* 344:513–520
- Di Carlo D, Irimia D, Tompkins RG, Toner M (2007) Continuous inertial focusing, ordering, and separation of particles in microchannels. *Proc Natl Acad Sci* 104:18892–18897
- Di Carlo D, Edd JF, Irimia D, Tompkins RG, Toner M (2008) Equilibrium separation and filtration of particles using differential inertial focusing. *Anal Chem* 80:2204–2211
- Doddabasavana G, PadmaPriya K, Nagabhusana K (2012) A review of recent advances in separation and detection of whole blood components. *World J Sci Technol* 2:05–09
- Dutta P, Beskok A (2001) Analytical solution of combined electroosmotic/pressure driven flows in two-dimensional straight channels: finite Debye layer effects. *Anal Chem* 73:1979–1986
- Figeys D, Pinto D (2000) Lab-on-a-chip: a revolution in biological and medical sciences. *Anal Chem* 72:330A–335A
- Gervang B, Larsen P (1991) Secondary flows in straight ducts of rectangular cross section. *J Non-Newtonian Fluid Mech* 39:217–237
- Ghosh U, Chakraborty S (2015) Electroosmosis of viscoelastic fluids over charge modulated surfaces in narrow confinements. *Phys Fluids* 27:062004
- Hashemabadi S, Etemad SG (2006) Effect of rounded corners on the secondary flow of viscoelastic fluids through non-circular ducts. *Int J Heat Mass Transfer* 49:1986–1990
- Haward SJ, Odell JA, Berry M, Hall T (2011) Extensional rheology of human saliva. *Rheol Acta* 50:869–879
- Hoffmann KA (1989) *Computational fluid dynamics for engineers*. Engineering Education System, Austin, p 1989
- Horiuchi K, Dutta P (2006) Heat transfer characteristics of mixed electroosmotic and pressure driven micro-flows. *JSME Int J B-Fluid T* 49:812–819
- Huang LR, Cox EC, Austin RH, Sturm JC (2004) Continuous particle separation through deterministic lateral displacement. *Science* 304:987–990
- Ireka I, Chinyoka T (2016) Analysis of shear banding phenomena in non-isothermal flow of fluids governed by the diffusive Johnson-Segalman model. *Appl Math Model* 40:3843–3859
- Jian Y-j, Liu Q-s, Yang L-g (2011) AC electroosmotic flow of generalized Maxwell fluids in a rectangular microchannel. *J Non-Newtonian Fluid Mech* 166:1304–1314
- Kandlikar S, Garimella S, Li D, Colin S, King MR (2005) *Heat transfer and fluid flow in minichannels and microchannels*. Elsevier, Amsterdam
- Karniadakis G, Beskok A, Aluru NR (2006) *Microflows and nanoflows: fundamentals and simulation*, vol 29. Springer, Berlin
- Kolodner P (1998) Oscillatory convection in viscoelastic DNA suspensions. *J Non-Newtonian Fluid Mech* 75:167–192
- Li D (2004) *Electrokinetics in microfluidics*, vol 2. Academic Press, London
- Lim H, Nam J, Shin S (2014) Lateral migration of particles suspended in viscoelastic fluids in a microchannel flow. *Microfluid Nanofluid* 17:683–692
- Maenaka H, Yamada M, Yasuda M, Seki M (2008) Continuous and size-dependent sorting of emulsion droplets using hydrodynamics in pinched microchannels. *Langmuir* 24:4405–4410
- Mai-Duy N, Tanner R (2005) Computing non-Newtonian fluid flow with radial basis function networks. *Int J Numer Meth Fluids* 48:1309–1336
- Maynes D, Webb B (2004) The effect of viscous dissipation in thermally fully-developed electro-osmotic heat transfer in microchannels. *Int J Heat Mass Tran* 47:987–999
- Nam J, Lim H, Kim D, Jung H, Shin S (2012) Continuous separation of microparticles in a microfluidic channel via the elasto-inertial effect of non-Newtonian fluid. *Lab Chip* 12:1347–1354
- Ng C-O (2013) Combined pressure-driven and electroosmotic flow of Casson fluid through a slit microchannel. *J Non-Newtonian Fluid Mech* 198:1–9
- Oldroyd J (1958) Non-Newtonian effects in steady motion of some idealized elasto-viscous liquids. *Proc R Soc Lon Ser-A* 245:278–297
- Oldroyd J (1965) Some steady flows of the general elasto-viscous liquid. In: *Proceedings of the royal society of London A: mathematical, physical and engineering sciences*, vol 1392. The Royal Society, London, pp 115–133
- Oliveira P (2002) An exact solution for tube and slit flow of a FENE-P fluid. *Acta Mech* 158:157–167
- Owens RG (2006) A new microstructure-based constitutive model for human blood. *J Non-Newtonian Fluid Mech* 140:57–70
- Park H, Lee W (2008a) Effect of viscoelasticity on the flow pattern and the volumetric flow rate in electroosmotic flows through a microchannel. *Lab Chip* 8:1163–1170
- Park H, Lee W (2008b) Helmholtz-Smoluchowski velocity for viscoelastic electroosmotic flows. *J Colloid Interface Sci* 317:631–636
- Phan-Thien N (1978) A nonlinear network viscoelastic model. *J Rheol* 22:259–283
- Poole R, Lindner A, Alves M (2013) Viscoelastic secondary flows in serpentine channels. *J Non-Newtonian Fluid Mech* 201:10–16
- Ramachandran A, Leighton DT (2008) The influence of secondary flows induced by normal stress differences on the shear-induced migration of particles in concentrated suspensions. *J Fluid Mech* 603:207–243

- Sadeghi A, Amini Y, Saidi MH, Chakraborty S (2014) Numerical modeling of surface reaction kinetics in electrokinetically actuated microfluidic devices. *Anal Chim Acta* 838:64–75
- Siline M, Leonov AI (2001) On flows of viscoelastic liquids in long channels and dies. *Int J Eng Sci* 39:415–437
- Sousa J, Afonso A, Pinho F, Alves M (2011) Effect of the skimming layer on electro-osmotic—Poiseuille flows of viscoelastic fluids. *Microfluid Nanofluid* 10:107–122
- Squires TM, Quake SR (2005) Microfluidics: fluid physics at the nanoliter scale. *Rev Mod Phys* 77:977
- Syrjälä S (1998) Laminar flow of viscoelastic fluids in rectangular ducts with heat transfer: a finite element analysis. *Int Commun Heat Mass Transfer* 25:191–204
- Tanoue S, Naganawa T, Iemoto Y (2006) Quasi-three-dimensional simulation of viscoelastic flow through a straight channel with a square cross section. *Nihon Reorogi Gakkaishi* 34:105–113
- Thien NP, Tanner RI (1977) A new constitutive equation derived from network theory. *J Non-Newtonian Fluid Mech* 2:353–365
- Townsend P, Walters K, Waterhouse W (1976) Secondary flows in pipes of square cross-section and the measurement of the second normal stress difference. *J Non-Newtonian Fluid Mech* 1:107–123
- Vakili MA, Sadeghi A, Saidi MH, Mozafari AA (2012) Electrokinetically driven fluidic transport of power-law fluids in rectangular microchannels. *Colloids Surf A Physicochem Eng Aspects* 414:440–456
- Vakili MA, Sadeghi A, Saidi MH (2014) Pressure effects on electroosmotic flow of power-law fluids in rectangular microchannels. *Theoret Comput Fluid Dyn* 28:409–426
- Vamerzani B, Norouzi M, Firoozabadi B (2014) Analytical solution for creeping motion of a viscoelastic drop falling through a Newtonian fluid Korea-Australia. *Rheol J* 26:91–104
- Villone M, D'Avino G, Hulsen M, Greco F, Maffettone P (2013) Particle motion in square channel flow of a viscoelastic liquid: migration vs. secondary flows. *J Non-Newtonian Fluid Mech* 195:1–8
- Vissink A, Waterman H, Panders A, Vermey A (1984) Rheological properties of saliva substitutes containing mucin, carboxymethylcellulose or polyethylenoxide. *J Oral Pathol Med* 13:22–28
- White FM, Corfield I (2006) *Viscous fluid flow*, vol 3. McGraw-Hill, New York
- Xue S-C, Phan-Thien N, Tanner R (1995) Numerical study of secondary flows of viscoelastic fluid in straight pipes by an implicit finite volume method. *J Non-Newtonian Fluid Mech* 59:191–213
- Yang C, Li D (1997) Electrokinetic effects on pressure-driven liquid flows in rectangular microchannels. *J Colloid Interface Sci* 194:95–107
- Yeleswarapu K, Kameneva M, Rajagopal K, Antaki J (1998) The flow of blood in tubes: theory and experiment. *Mech Res Commun* 25:257–262
- Yoon DH, Ha JB, Bahk YK, Arakawa T, Shoji S, Go JS (2009) Size-selective separation of micro beads by utilizing secondary flow in a curved rectangular microchannel. *Lab Chip* 9:87–90
- Yue P, Dooley J, Feng JJ (2008) A general criterion for viscoelastic secondary flow in pipes of noncircular cross section. *J Rheol (1978-present)* 52:315–332
- Zhang J, Li M, Li W, Alici G (2013) Inertial focusing in a straight channel with asymmetrical expansion–contraction cavity arrays using two secondary flows. *J Micromech Microeng* 23:085023
- Zimmerman W, Rees J, Craven T (2006) Rheometry of non-Newtonian electrokinetic flow in a microchannel T-junction. *Microfluid Nanofluid* 2:481–492